Received: 1 September 2021 | Revised: 19 January 2022 | Accepted: 21 January 2022

DOI: 10.1002/glia.24154

GLIA

WILEY

RESEARCH ARTICLE

Wasl is crucial to maintain microglial core activities during glioblastoma initiation stages

Julie Mazzolini[1] | Sigrid Le Clerc[2] | Gregoire Morisse[1] | Cédric Coulonges[2] | Jean-François Zagury[2] | Dirk Sieger[1]

[1]Centre for Discovery Brain Sciences, University of Edinburgh, Edinburgh, UK

[2]Laboratoire GBCM, EA7528, Conservatoire National des Arts et Métiers, HESAM Université, Paris, France

Correspondence
Julie Mazzolini and Dirk Sieger, Centre for Discovery Brain Sciences, 49 Little France Crescent, Edinburgh EH16 4SB, UK.
Email: julie.mazzolini@ed.ac.uk and dirk.sieger@ed.ac.uk

Funding information
Cancer Research UK, Grant/Award Number: C49916/A17494

Abstract

Microglia actively promotes the growth of high-grade gliomas. Within the glioma microenvironment an amoeboid microglial morphology has been observed, however the underlying causes and the related impact on microglia functions and their tumor promoting activities is unclear. Using the advantages of the larval zebrafish model, we identified the underlying mechanism and show that microglial morphology and functions are already impaired during glioma initiation stages. The presence of pre-neoplastic HRasV12 expressing cells induces an amoeboid morphology of microglia, increases microglial numbers and decreases their motility and phagocytic activity. RNA sequencing analysis revealed lower expression levels of the actin nucleation promoting factor *wasla* in microglia. Importantly, a microglia specific rescue of *wasla* expression restores microglial morphology and functions. This results in increased phagocytosis of pre-neoplastic cells and slows down tumor progression. In conclusion, we identified a mechanism that de-activates core microglial functions within the emerging glioma microenvironment. Restoration of this mechanism might provide a way to impair glioma growth.

KEYWORDS
microglia, glioblastoma, *wasl*, RNA sequencing, morphology, cytoskeleton, phagocytosis

1 | INTRODUCTION

High-grade gliomas represent a complex and devastating disease and are posing an unmet clinical need. These tumors resist multimodal therapies and survival times are only 14 months on average (Gregory et al., 2020; Kadiyala et al., 2019; Lucki et al., 2019; Wen & Kesari, 2008). In recent years, a lot of focus has been on the complex microenvironment of gliomas. Microglia and infiltrating macrophages are the most prominent cell types within the glioma microenvironment and can account for up to 30%–50% of the total tumor mass (for review see (Hambardzumyan et al., 2015; Quail & Joyce, 2017). Instructed by a variety of chemokines and cytokines microglia actively promote tumor growth by affecting processes such as cell proliferation and invasiveness, extracellular matrix modifications, angiogenesis and the formation of an immunosuppressive environment (Ellert-Miklaszewska et al., 2013; Hambardzumyan et al., 2015; Komohara et al., 2008; Markovic et al., 2005; Pyonteck et al., 2013; H. Wang et al., 2013; Wu et al., 2010; Zhai et al., 2011; Zhang et al., 2012). Interestingly, these pro-tumoral functions seem to be independent of the tumor grade, as they have also been described for low-grade gliomas (Costa et al., 2021; Daginakatte et al., 2008; Daginakatte & Gutmann, 2007; Guo et al., 2019; Simmons et al., 2011).

While these processes have been described in gliomas, surprisingly little is known about the apparent change of morphology of

microglia within the glioma and the possible impact on their functions. Microglia, as the resident innate immune cells of the brain, display unique morphological features. Under physiological conditions microglia are in a surveillance mode and actively and continuously scan their microenvironment using dynamic large processes providing them a ramified morphology (Nimmerjahn et al., 2005). However, once the homeostasis is altered by injury or brain pathologies, microglia retract their processes to acquire an amoeboid shape. This change in morphology can correlate with an either anti- or pro-inflammatory state of microglia (Bernier et al., 2019; Bolasco et al., 2018; Chia et al., 2018; Karperien, 2013; Kettenmann et al., 2011; Lawson et al., 1992; Madry, Arancibia-Cárcamo, et al., 2018; Madry, Kyrargyri, et al., 2018). Of note, an amoeboid microglial morphology has been observed in vivo across different glioma models at different stages of glioma growth as well as within human glioma samples (Annovazzi et al., 2018; Chia et al., 2018; Juliano et al., 2018; Kvisten et al., 2019; Resende et al., 2016; Ricard et al., 2016). Furthermore, these microglia show a decreased phagocytic activity and motility within the central area of neoplastic lesions (Hutter et al., 2019; Jaiswal et al., 2009; Juliano et al., 2018; Pyonteck et al., 2013; Wu et al., 2010). The mechanisms underlying this rapid and drastic morphological remodeling are still not known. Clearly, these morphological phenotypes must be highly regulated and involve adaptations to the cellular cytoskeleton (Bernier et al., 2019; Okazaki et al., 2020). Cell morphology, phagocytosis and motility are cellular processes known to be actin-dependent and are crucial for the multitasking roles of microglia (Koizumi et al., 2007; Liu et al., 2020; Lively & Schlichter, 2013; Okazaki et al., 2020; Pollard & Cooper, 2009; Uhlemann et al., 2015). An alteration of the microglial actin cytoskeleton and their morphology will most likely affect several of these core functions. Therefore, it is important to understand the impact of an amoeboid microglial morphology on their functions within the tumor microenvironment and its effects on tumor growth.

Here, we investigated the influence of a pre-neoplastic glioma environment on microglia morphology and related functions. We utilized a recently published zebrafish glioblastoma multiforme (GBM) model which is based on expression of the human oncogene HRasV12 in the proliferating domains of the developing brain and gives rise to tumors similar to the mesenchymal subtype of human GBM (Mayrhofer et al., 2017). Analysing larval stages of this zebrafish model allowed us to directly study, the influence of an early pre-neoplastic environment on the morphology and functions of microglia in vivo. Importantly, we detected an immediate impact of pre-neoplastic HRasV12^{+} cells on the microglia population resulting in an amoeboid phenotype and increased proliferation of the microglia. Furthermore, their phagocytic activity, motility and speed was significantly reduced compared to control microglia. RNA sequencing of microglia revealed significantly lower expression levels of *wasla*, the zebrafish orthologue of human WASP like actin nucleation promoting factor (WASL, also known as N-WASP), a key regulator of actin cytoskeleton organization (Dart et al., 2012; Linder et al., 1999; Lorenz et al., 2004; Park & Cox, 2009; Yamaguchi et al., 2005; Yu et al., 2012). Importantly, a microglia specific rescue of *wasla* expression in HRasV12^{+} larvae restored microglial morphology as well as their number, speed and motility. Furthermore, the *wasla* rescue in microglia restored their phagocytic activity which resulted in improvements in both engulfment of pre-neoplastic cells and survival.

2 | METHODS

Key resources table Reagent type (species) or resource	Designation	Source or reference	Identifiers	Additional information
Antibody	anti-4C4 (mouse monoclonal)	Sieger Laboratory, University of Edinburgh		IHC (1:50) FACS (1:20)
Antibody	Alexa 488- or 647 secondaries	Life Technologies	Life Technologies A11029 (RRID: AB_2534088) A21236 (RRID: AB_2535805)	(1:200)
Commercial assay or kit	RNeasy Plus Micro Kit	QIAGEN	QIAGEN: 74034	
Commercial assay or kit	Quant-iT™ RiboGreen™ RNA Assay Kit	Invitrogen	Invitrogen: R11490	
Commercial assay or kit	Agilent RNA 6000 Pico kit	Agilent	Agilent: 5067-1513	
Commercial assay or kit	SsoAdvanced™ Universal SYBR® Green Supermix	Bio-Rad	Bio-Rad: 1725271	
Commercial assay or kit	SuperScript® III First-Strand Synthesis System	Invitrogen	Invitrogen: 18080-051	
Commercial assay or kit	Ovation RNA-Seq System V2 kit NuGen	NuGen	NuGen: 3100-A01	
Chemicals	Zymosan	Merck	Merck: Z4250	

Key resources table Reagent type (species) or resource	Designation	Source or reference	Identifiers	Additional information
Chemicals	Pacific blue	Invitrogen	Invitrogen: P10163	
Gene (Danio rerio)	wasla	N/A	ZDB-GENE-070209-220	
Gene (Danio rerio)	mpeg1	N/A	ZDB-GENE-030131-7347	
Recombinant DNA reagent	pDEST (Gateway vector)	Invitrogen		
Recombinant DNA reagent	mpeg1:wasla	This article	Tol2-pDEST-mpeg1:wasla-pA	Gateway vector: pDEST
Recombinant DNA reagent	UAS:TagBFP2	This article	Tol2-pDEST-UAS-TagBFP2-pA	Gateway vector: pDEST
Recombinant DNA reagent	UAS:myrAKT1-UAS:BFP	This article	Tol2-pDEST-UAS-myrAkt1-UAS-BFP	Gateway vector: pDEST
recombinant DNA reagent	UAS:BRAF-V600E	This article	Tol2-pDEST-UAS-BRAF-V600E-pA	Gateway vector: pDEST
Recombinant DNA reagent	zic1:GAL4TA4,VP16	PMID: 17279576	zic1:Gal4VP16 PAC DNA	vector: PAC
Strain, strain background (Danio rerio)	mpeg1:mCherry	PMID: 21084707	Tg(mpeg1:mCherry)gl23, RRID:ZIRC_ZL9939	
Strain, strain background (Danio rerio)	HRasV12-	PMID: 19628697	Et(zic4:GAL4TA4,UAS:mCherry)hmz RRID:ZFIN: ZDB-ETCONSTRCT-110214-1	
Strain, strain background (Danio rerio)	UAS:eGFP-HRASv12	PMID: 21170325	Tg(UAS:eGFP-HRASv12)io006 RRID:ZFIN: ZDB-TGCONSTRCT-090702-1	
Strain, strain background (Danio rerio)	Tg(UAS:TagBFP2-HRASv12)	This article	Tg(UAS:TagBFP2-HRASv12	
Strain, strain background (Danio rerio)	Tg(zic1:Gal4 VP16/UAS:GFP)	PMID: 17279576	Tg(zic1:Gal4VP16/UAS:GFP)	
Strain, strain background (Danio rerio)	Tg(zic4:Gal4 UAS:mCherry: mpeg1:eGFP)	This article	Tg(zic4:Gal4UAS:mCherry: mpeg1:eGFP)	
Strain, strain background (Danio rerio)	Tg(zic1:GAL4 TA4,VP16)	PMID: 17279576	Tg(zic1:GAL4TA4,VP16) RRID:ZFIN: ZDB-TGCONSTRCT-070521-2	
Software, algorithm	Imaris 8.0.2	Bitplane	RRID:SCR_007370	
Software, algorithm	LightCycler® 96 Software	Roche	RRID:SCR_012155	
Software, algorithm	GraphPad PRISM	GraphPad Software	N/A	

2.1 | Zebrafish maintenance

Animal experimentation was approved by the ethical review committee of the University of Edinburgh and the Home Office, in accordance with the Animal (Scientific Procedures) Act 1986. Zebrafish were housed in a purpose-built zebrafish facility, in the Queen's Medical Research Institute, maintained by the University of Edinburgh Biological Resources. All zebrafish larvae were kept at 28°C on a 14 h light/10 h dark photoperiod. Embryos were obtained by natural spawning from adult *Et(zic4:GAL4TA4,UAS:mCherry)*$_{hmz5}$ referred to as HRasV12^{-} (Distel et al., 2009), *Tg(zic1:GAL4TA4,UAS:eGFP)* (Sassa et al., 2007), *Tg(UAS:eGFP-HRasV12)*$_{io006}$ (Santoriello et al., 2010), *Tg (mpeg1:mCherry*; Ellett et al., 2011), *Tg(zic4:Gal4UAS:mCherry:mpeg1: eGFP)*, *Tg(UAS:TagBFP2-HRasV12)*, *Tg(zic1:GAL4TA4,VP16)*, and wild-type (WIK) zebrafish strains. Table 1 provides details of the use of the individual lines for the different assays. Embryos were raised at

TABLE 1 Experimental fish models

	HRasV12-	Microinjection	HRasV12+	Microinjection	Other fish lines	Microinjection
Figure 1a	/	/	Et(zic4:GAL4TA4,UAS:mCherry)$_{hmz5}$ x Tg(UAS:eGFP-HRasV12)io006	/	/	/
Figure 1b	Et(zic4:GAL4TA4,UAS:mCherry)$_{hmz5}$ x Et(zic4:GAL4TA4,UAS:mCherry)hmz5	/	Et(zic4:GAL4TA4,UAS:mCherry)$_{hmz5}$ x Tg(UAS:eGFP-HRasV12)io006	/	/	/
Figure 1c	Et(zic4:GAL4TA4,UAS:mCherry)$_{hmz5}$ x Et(zic4:GAL4TA4,UAS:mCherry)hmz5	/	Et(zic4:GAL4TA4,UAS:mCherry)$_{hmz5}$ x Tg(UAS:eGFP-HRasV12)io006	/	/	/
Figure 1d	Et(zic4:GAL4TA4,UAS:mCherry)$_{hmz5}$ x Et(zic4:GAL4TA4,UAS:mCherry)hmz5	/	Et(zic4:GAL4TA4,UAS:mCherry)$_{hmz5}$ x Tg(UAS:eGFP-HRasV12)io006	/	/	/
Figure 2a	Et(zic4:GAL4TA4,UAS:mCherry)$_{hmz5}$ x Et(zic4:GAL4TA4,UAS:mCherry)hmz5	/	Et(zic4:GAL4TA4,UAS:mCherry)$_{hmz5}$ x Tg(UAS:eGFP-HRasV12)io006	/	/	/
Figure 2b	Tg(zic1:GAL4TA4,VP16) x Tg(zic1:GAL4TA4,VP16)	/	Tg(zic1:GAL4TA4,VP16) x Tg(UAS:TagBFP2-HRasV12)	/	/	/
Figure 3a	Et(zic4:GAL4TA4,UAS:mCherry)$_{hmz5}$ x Et(zic4:GAL4TA4,UAS:mCherry)hmz5	/	Et(zic4:GAL4TA4,UAS:mCherry)$_{hmz5}$ x Tg(UAS:eGFP-HRasV12)io006	/	/	/
Figure 3b	Et(zic4:GAL4TA4,UAS:mCherry)$_{hmz5}$ x Et(zic4:GAL4TA4,UAS:mCherry)hmz5	/	Et(zic4:GAL4TA4,UAS:mCherry)$_{hmz5}$ x Tg(UAS:eGFP-HRasV12)io006	/	/	/
Figure 3c	Tg(zic4:Gal4UAS:mCherry:mpeg1:eGFP) x Tg(zic4:Gal4UAS:mCherry:mpeg1:eGFP)	/	Tg(zic4:Gal4UAS:mCherry:mpeg1:eGFP) x Tg(UAS:TagBFP2-HRasV12)	/	/	/
Figure 3d	Tg(zic4:Gal4UAS:mCherry:mpeg1:eGFP) x Tg(zic4:Gal4UAS:mCherry:mpeg1:eGFP)	/	Tg(zic4:Gal4UAS:mCherry:mpeg1:eGFP) x Tg(UAS:TagBFP2-HRasV12)	/	/	/
Figure 4a	Et(zic4:GAL4TA4,UAS:mCherry)$_{hmz5}$ x Et(zic4:GAL4TA4,UAS:mCherry)hmz5	/	Et(zic4:GAL4TA4,UAS:mCherry)$_{hmz5}$ x Tg(UAS:eGFP-HRasV12)io006	/	/	/
Figure 4b	Et(zic4:GAL4TA4,UAS:mCherry)$_{hmz5}$ x Et(zic4:GAL4TA4,UAS:mCherry)hmz5	/	Et(zic4:GAL4TA4,UAS:mCherry)$_{hmz5}$ x Tg(UAS:eGFP-HRasV12)io006	/	/	/
Figure 5a	Et(zic4:GAL4TA4,UAS:mCherry)$_{hmz5}$ x Et(zic4:GAL4TA4,UAS:mCherry)hmz5	/	Et(zic4:GAL4TA4,UAS:mCherry)$_{hmz5}$ x Tg(UAS:eGFP-HRasV12)io006	Tol2-pDEST-mpeg1:wasla-pA	/	/
	Tg(zic4:Gal4UAS:mCherry:mpeg1:eGFP) x Tg(zic4:Gal4UAS:mCherry:mpeg1:eGFP)	/	Tg(zic4:Gal4UAS:mCherry:mpeg1:eGFP) x Tg(UAS:TagBFP2-HRasV12)	Tol2-pDEST-mpeg1:wasla-pA	/	/
Figure 5b	Et(zic4:GAL4TA4,UAS:mCherry)$_{hmz5}$ x Et(zic4:	/			/	/

TABLE 1 (Continued)

	HRasV12-	Microinjection	HRasV12+	Microinjection	Other fish lines	Microinjection
	GAL4TA4,UAS:mCherry) hmz5		Et(zic4:GAL4TA4,UAS:mCherry)$_{hmz5}$ x Tg(UAS:eGFP-HRasV12)io006	Tol2-pDEST-mpeg1:wasla-pA		
Figure 5c	Et(zic4:GAL4TA4,UAS:mCherry)$_{hmz5}$ x Et(zic4:GAL4TA4,UAS:mCherry) hmz5	/	Et(zic4:GAL4TA4,UAS:mCherry)$_{hmz5}$ x Tg(UAS:eGFP-HRasV12)io006	Tol2-pDEST-mpeg1:wasla-pA	/	/
Figure 5d	Et(zic4:GAL4TA4,UAS:mCherry)$_{hmz5}$ x Et(zic4:GAL4TA4,UAS:mCherry) hmz5	/	Et(zic4:GAL4TA4,UAS:mCherry)$_{hmz5}$ x Tg(UAS:eGFP-HRasV12)io006	Tol2-pDEST-mpeg1:wasla-pA	/	/
	Tg(zic4:Gal4UAS:mCherry:mpeg1:eGFP) x Tg(zic4:Gal4UAS:mCherry:mpeg1:eGFP)	/	Tg(zic4:Gal4UAS:mCherry:mpeg1:eGFP) x Tg(UAS:TagBFP2-HRasV12)	Tol2-pDEST-mpeg1:wasla-pA	/	/
Figure 6a	Et(zic4:GAL4TA4,UAS:mCherry)$_{hmz5}$ x Et(zic4:GAL4TA4,UAS:mCherry) hmz5	/	Et(zic4:GAL4TA4,UAS:mCherry)$_{hmz5}$ x Tg(UAS:eGFP-HRasV12)io006	Tol2-pDEST-mpeg1:wasla-pA	/	/
Figure 6b	Et(zic4:GAL4TA4,UAS:mCherry)$_{hmz5}$ x Et(zic4:GAL4TA4,UAS:mCherry) hmz5	/	Et(zic4:GAL4TA4,UAS:mCherry)$_{hmz5}$ x Tg(UAS:eGFP-HRasV12)io006	Tol2-pDEST-mpeg1:wasla-pA	/	/
Figure 6c	/	/	Et(zic4:GAL4TA4,UAS:mCherry)$_{hmz5}$ x Tg(UAS:eGFP-HRasV12)io006	/	/	/
	/	/	Et(zic4:GAL4TA4,UAS:mCherry)$_{hmz5}$ x Tg(UAS:eGFP-HRasV12)io006	Tol2-pDEST-mpeg1:wasla-pA	/	/
Figure 6d	/	/	Et(zic4:GAL4TA4,UAS:mCherry)$_{hmz5}$ x Tg(UAS:eGFP-HRasV12)io006	/	/	/
	/	/	Et(zic4:GAL4TA4,UAS:mCherry)$_{hmz5}$ x Tg(UAS:eGFP-HRasV12)io006	Tol2-pDEST-mpeg1:wasla-pA	/	/
Figure S1A	Et(zic4:GAL4TA4,UAS:mCherry)$_{hmz5}$ x Et(zic4:GAL4TA4,UAS:mCherry) hmz5	/	Et(zic4:GAL4TA4,UAS:mCherry)$_{hmz5}$ x Tg(UAS:eGFP-HRasV12)io006	/	/	/
Figure S1B	Et(zic4:GAL4TA4,UAS:mCherry)$_{hmz5}$ x Et(zic4:GAL4TA4,UAS:mCherry) hmz5	/	Et(zic4:GAL4TA4,UAS:mCherry)$_{hmz5}$ x Tg(UAS:eGFP-HRasV12)io006	/	/	/
Figure S1E	Tg(zic4:Gal4UAS:mCherry:mpeg1:eGFP) x Tg(zic4:Gal4UAS:mCherry:mpeg1:eGFP)	/	Tg(zic4:Gal4UAS:mCherry:mpeg1:eGFP) x Tg(UAS:TagBFP2-HRasV12)	/	/	/
Figure S2	Et(zic4:GAL4TA4,UAS:mCherry)$_{hmz5}$ x Et(zic4:GAL4TA4,UAS:mCherry) hmz5	/	Et(zic4:GAL4TA4,UAS:mCherry)$_{hmz5}$ x Tg(UAS:eGFP-HRasV12)io006	/	/	/
Figure S3	Et(zic4:GAL4TA4,UAS:mCherry)$_{hmz5}$ x Et(zic4:GAL4TA4,UAS:mCherry) hmz5	/	Et(zic4:GAL4TA4,UAS:mCherry)$_{hmz5}$ x Tg(UAS:eGFP-HRasV12)io006	/	/	/

(Continues)

TABLE 1 (Continued)

	HRasV12-	Microinjection	HRasV12+	Microinjection	Other fish lines	Microinjection
Figure S4A	/	/	/	/	Tg(mpeg1:mCherry)	/
	/	/	/	/	Tg(mpeg1:mCherry)	Tol2-pDEST-mpeg1:wasla-pA
Figure S4B	/	/	/	/	Tg(mpeg1:mCherry)	/
	/	/	/	/	Tg(mpeg1:mCherry)	Tol2-pDEST-mpeg1:wasla-pA
Figure S4C	Et(zic4:GAL4TA4,UAS:mCherry)$_{hmz5}$ x Et(zic4:GAL4TA4,UAS:mCherry)hmz5	/	/	/	/	/
	Et(zic4:GAL4TA4,UAS:mCherry)$_{hmz5}$ x Et(zic4:GAL4TA4,UAS:mCherry)hmz5	Tol2-pDEST-mpeg1:wasla-pA	/	/	/	/
Figure S5	Tg(zic4:Gal4UAS:mCherry:mpeg1:eGFP) x Tg(zic4:Gal4UAS:mCherry:mpeg1:eGFP)	/	/	/	/	/
	myrAKT1-	Microinjection	AKT1+	Microinjection	Other fish lines	Microinjection
Figure S1C	Et(zic4:GAL4TA4,UAS:mCherry)$_{hmz5}$ x Et(zic4:GAL4TA4,UAS:mCherry)hmz5	Tol2-pDEST-UAS-TagBFP2-pA	Et(zic4:GAL4TA4,UAS:mCherry)$_{hmz5}$ x Et(zic4:GAL4TA4,UAS:mCherry)hmz5	Tol2-pDEST-UAS-myrAkt1-UAS-BFP	/	/
	BRAFV600E-	Microinjection	BRAFV600E+	Microinjection	Other fish lines	Microinjection
Figure S1D	Et(zic4:GAL4TA4,UAS:mCherry)$_{hmz5}$ x Et(zic4:GAL4TA4,UAS:mCherry)hmz5	/	Et(zic4:GAL4TA4,UAS:mCherry)$_{hmz5}$ x Et(zic4:GAL4TA4,UAS:mCherry)hmz5	Tol2-pDEST-UAS-BRAFV600E-pA	/	/

28.5°C in embryo medium (E3) and treated with 200 μM 1-phenyl 2-thiourea (PTU) (Sigma) from the end of the first day of development for the duration of the experiment to prevent pigmentation.

2.2 | DNA injection to overexpress myrAKT1, BRAF-V600E and *wasla*

To generate transient expression of either myrAKT1 or BRAF-V600E in radial glial progenitor cells of HRasV12^{-} larvae, and *wasla* in microglia/macrophages of HRasV12^{-}, HRasV12^{+} and *Tg(mpeg1:mCherry)* larvae, zebrafish embryos were injected at the one cell stage using an Eppendorf FemtoJet microinjector. Approximately 2 nl of injection solution containing either 60 ng/μl of Tol2-pDEST-UAS-TagBFP2-pA (myrAKT1^{-}), Tol2-pDEST-UAS-myrAkt1-UAS-BFP (myrAKT1^{+}), Tol2-pDEST-UAS-BRAF-V600E-pA (BRAF-V600E^{+}) plasmid, or 30 ng/μl of Tol2-pDEST-mpeg1:wasla-pA plasmid, 20 ng/μl Tol2 capped mRNA and 0.1% phenol red were respectively injected into HRasV12^{-}, HRasV12^{+} and *Tg(mpeg1:mCherry)* eggs. Larvae were screened at 2 days post-fertilization (dpf) for positive transgene expression and selected for the required experiments.

2.3 | Mounting, immunohistochemistry, image acquisition and live imaging

Whole-mount immunostaining of samples was performed as previously described (Astell & Sieger, 2017). Briefly, larvae were fixed in 4% PFA/1% DMSO in PBS at room temperature (RT °C) for 2 h, then washed in PBStx (0.2% Triton X-100 in 0.01M PBS) and blocked in 1% goat serum blocking buffer (1% normal goat serum, 1% DMSO, 1% BSA, and 0.7% Triton X-100 in 0.01 M PBS) for 2 h prior to incubation with the mouse anti-4C4 primary antibody [1:50] overnight at 4°C to stain microglia. Samples were washed in PBStx before their

incubation with conjugated secondary antibodies (goat anti-mouse Alexa Fluor 647 [1:200]) (Life Technologies) overnight at 4°C. The samples were washed several times with PBStx and stored in 70% glycerol at 4°C until final mounting in 1.5% low melting point agarose (Life Technologies) in E3 for image acquisition. Whole-brain immunofluorescent images were acquired using confocal laser scanning microscopy (Zeiss LSM710 and LSM880; ×20 objective (air, NA = 0.8); z-step = 1.69 μm; 405 nm, 488 nm, 594 nm, 633 nm laser lines).

Live imaging of zebrafish larvae was performed as previously described (Chia et al., 2018); samples were anaesthetized with 450 μM Tricaine (MS222, Sigma) and mounted dorsal side up in 1.5% low melting point agarose (Life Technologies), in 60 x 15 mm petri dishes (Corning) filled with E3 containing 450 μM Tricaine and 200 μM PTU. To investigate microglia motility and phagocytosis from 3 and 5 dpf HRasV12^{-}, HRasV12^{+} and HRasV12^{+}; wasla larval brains, time-lapse imaging with Z stacks were acquired using a Zeiss LSM880 confocal microscope equipped with an Airyscan Fast module and a piezo z-drive (Zeiss Plan-Apochromat ×20 (water, NA = 1.0); z-step = 1.5 μm). All time-lapse acquisitions were carried out in temperature-controlled climate chambers set to 28°C for 13 h with acquisition every 14 min.

2.4 | Proliferation assay (EdU staining)

Proliferation assay was performed following guidance of the Click-iT™ EdU Cell Proliferation Kit for Imaging, Alexa Fluor™ 647 dye (Invitrogen). Briefly, embryos were collected from the outcross of the driver fish line *Tg(zic4:GAL4TA4,VP16)* to the *Tg(UAS:TagBFP2-HRasV12)* fish lines. At 2 dpf dechorionated HRasV12^{-} and HRasV12^{+} larvae were incubated with EdU (50 μM) in E3 containing 200 μM PTU then raised at 28.5°C. At 5 dpf larvae were fixed in 4% PFA/1%DMSO in PBS at RT °C for 2 h, washed several times in PBStx, digested with collagenase (Sigma) at 2 mg/ml in PBS at RT °C for 40 min under agitation, washed in PBStx then incubated in Click-iT reaction cocktail at RT °C for 4 h under agitation. Larvae were washed in PBStx then blocked in 1% goat serum blocking buffer to carry out microglia immunostaining as described in previous paragraph.

2.5 | Phagocytosis assay

Phagocytosis assay was performed using an Eppendorf FemtoJet microinjector to inject custom made zymosan (Sigma) coupled with Pacific Blue fluorochrome (molecular probes) into the larval zebrafish brain. Anesthetized 3 and 5 dpf HRasV12^{-}, HRasV12^{+} and HRasV12^{+}; wasla larvae were injected into either telencephalon or tectum with approximately 2 nl of injection solution composed of 2.5.10^{5} zymosan/μl, 0.1% phenol red in PBS. Injected larvae were maintained at 28.5°C in E3 containing 200 μM PTU for 6 h, fixed in 4% PFA/1% DMSO in PBS at RT °C for 2 h then microglia immunostaining was performed. Phagocytosis of pre-neoplastic HRasV12^{+} cells by microglia is described in the microglia/macrophage isolation section.

2.6 | Image analysing

Analysis of all images was performed in 3D using Imaris (Bitplane, Zurich, Switzerland). To assess microglia (4C4^{+}) morphology and volume measurements, we used the surface-rendering tool in Imaris 8.2.1, which allowed segmentation of individual cells in 3D as well as bigger volumes such as brain and pre-neoplastic mass volume. To assess microglia morphological changes, we calculated the ratio of the cellular surface and cellular volume of individual cells as previously described (Chia et al., 2018; Gyoneva et al., 2014). Microglia with a ratio smaller than 0.8 were classified as amoeboid. The "Spots" function tool was used to quantify the number of amoeboid microglia related to the total number of microglia within the full brain, and the averaged value expressed as measure of the percentage of amoeboid microglia. To determine the percentage of infiltrated macrophages and microglia at 5 dpf, a 4C4 immunostaining was performed on HRasV12^{-} and HRasV12^{+} larvae with GFP^{+} macrophages and microglia (mpeg1:GFP). The number of 4C4^{+}/GFP^{+} cells (microglia) and 4C4^{-}/GFP^{+} cells (macrophages) were counted in relation to the total number of myeloid cells (microglia + macrophages) within the full brain and the averaged value expressed as measure of percentage of macrophages and microglia.

To quantify proliferation rates, the number of 4C4^{+}/EdU^{+} cells (EdU^{+} microglia) were counted in relation to the total number of microglia within the full brain and the averaged value expressed as a measure of percentage of microglia proliferation. To quantify zymosan phagocytosed by microglia of 3 and 5 dpf HRasV12^{-}, HRasV12^{+} and HRasV12^{+}; wasla larval brains, we used the surface-rendering tool in Imaris 8.2.1 to manually create a surface corresponding to the fluorescent signal of all zymosan particles. An additional surface for microglia allowed us to distinguish zymosan that had been phagocytosed by microglia. This allowed us to read out the sum of fluorescence intensity (AU) of phagocytosed zymosan within microglia surfaces and the total AU of all zymosan surfaces. The percentage of microglia phagocytosis was calculated from the averaged value of the number of phagocytosed zymosan related to the total number of zymosan within either the telencephalon or the tectum (Engulfed zymosan fluorescent intensity:total zymosan fluorescent intensity) x 100).

To assess microglia motility of 3 and 5 dpf HRasV12^{-}, HRasV12^{+} and HRasV12^{+}; wasla larval brains, we used the "Tracking" function tool and manually tracked mpeg:eGFP^{+} cells along time. Imaris software calculated track length and track speed mean for each cell and microglia tracks were displayed as time color-coded lines for the different conditions. To measure the number of phagosomes per microglia from 5 dpf HRasV12^{+} and HRasV12^{+}; wasla larvae, we used mpeg1:eGFP^{+} cells to visualize phagosomes in black within GFP^{+} cytoplasm. The combination of 3D and slide views on Imaris software allowed us to manually count the number of phagosomes in microglia within the tectum of 10 larvae per condition.

2.7 | Microglia/macrophage isolation

Microglia were isolated by FACS from 3 and 5 dpf heads of HRasV12^{-} and HRasV12^{+} larvae as previously described (Mazzolini et al., 2018) whereas microglia and macrophages were isolated from whole 5 dpf mpeg1:mCherry^{+} and mpeg1:mCherry^{+}; wasla larvae. FACS allowed cell separation from debris in function of their size (FSC-A) and granularity (SSC-A). Single cells were then separated from doublets or cell agglomerates (FSC Singlet; SSC Singlet). From the single-cell population, a gate was drawn to separate live cells (DAPI−) from dead cells (DAPI+). Unstained and cells incubated with secondary antibody Alx647 only were used as controls to draw gates corresponding to microglia (4C4^{+}/Alx647^{+}) populations. Finally, microglia (4C4^{+}/Alx647^{+}; Figure S2) and microglia/macrophage (mCherry^{+}; Figure S4A) were segregated from the live cell population gates. FACS data were analysed using FlowJo Software (Treestar, Ashland, OR).

Phagocytosis of pre-neoplastic HRasV12^{+} cells by microglia was measured using the mean of GFP fluorescent intensity from HRasV12^{+} cells detected within isolated microglia from 5 dpf HRasV12^{+} and HRasV12^{+}; wasla larvae.

2.8 | RNA extraction and cDNA amplification

All experiments were performed in three replicates with a total number of 600 larvae per replicate. Total RNA extraction from microglial cells was performed using the Qiagen RNeasy Plus Micro kit according to the manufacturer's guidance (Qiagen). RNA sample quality and concentration were determined using Agilent RNA 6000 Pico kit and an Agilent 2100 Bioanalyser System (Agilent Technologies).

For sequencing, all RNA samples with a RIN score >7 were transcribed into cDNA using the Ovation RNA-Seq System V2 kit according to the manufacturer's instructions (NuGEN). Samples were then sent to Edinburgh Genomics for library synthesis and sequencing. For qPCR, RNA sample quality and concentration were assessed using the LabChip GX Touch Nucleic Acid Analyzer and RNA Pico Sensitivity Assay. All RNA samples with a RIN score >7 were transcribed from the same amount of RNA into cDNA using the SuperScript® III First-Strand Synthesis System (Invitrogen).

2.9 | Library synthesis

Sequencing libraries were prepared using the Illumina TruSeq DNA Nano library preparation kit according to manufacturer's instructions with amended shearing conditions (duty factor 10%, PIP 175, cycles/burst 200, duration 40 s) using a 500 ng input of amplified cDNA (Illumina, Inc.). The size selection for the sheared cDNA was set for 350 bp products. Libraries were normalized and ran on 2 HiSeq 4000 lanes with 75-base paired-end reads resulting in an average read depth of around 20 million read pairs per sample.

2.10 | Bioinformatics

The quality control of the sequences was done with FastQC (Andrews, 2010), and Trimmomatic was applied to trim low-quality reads and adapters (Bolger et al., 2014). We aligned the RNA-seq reads to the zebrafish reference genome (Ensembl, GRCz11) using STAR v2.6 (Dobin et al., 2013) and transcript were assembled and counted with HTSeq (Anders et al., 2015) using annotation from Ensembl (Danio_rerio.GRCz11.93.gtf). Count normalization, transformation (rlog) and differential expression analysis were performed using DESeq2 (Love et al., 2014). Normalized data were inspected using principal component analysis (PCA; Figure S3B), and inter-sample correlation plots (Figure S3A). We selected genes related to actin cytoskeleton among the KEGG database: dre04810 "Regulation of actin cytoskeleton," dre04510 "Focal adhesion," dre04520 "Adherens junction," dre04150 "mTOR signalling pathway," and dre04530 "Tight junction" (Kanehisa & Goto, 2000). We performed the gene expression comparison between isolated microglia from 3 dpf and 5 dpf HRasV12^{-} and HRasV12^{+} larvae using DESeq2. Finally, we looked for top ranked genes differentially expressed at 5 dpf and constant at 3 dpf in HRasV12^{-} and HRasV12^{+} microglia, for further investigations.

The expression data and clinical annotation for human glioma samples were downloaded from the Joyce Lab Brain TIME database (Klemm et al., 2020). We retrieved raw count data for MDMs and microglia. The raw counts were normalized and transformed (rlog) using DESeq2 (Love et al., 2014). Eventually, we compared *WASL* expression of MDMs and microglia from human non-tumor and glioma IDH WT brain samples with DESeq2 (Love et al., 2014).

2.11 | Quantitative PCR

Quantitative (qPCR) amplifications were performed in technical triplicates in a 20 μl reaction volume containing SsoAdvanced Universal SYBR Green Supermix (Bio-Rad) using a LightCycler 96 Real-Time PCR System (Roche). The PCR protocol used was initial denaturation step of 10 min at 95°C, and 45 cycles of 10 s at 95°C, 20 s at 56°C, and 20 s at 72°C. Primers used were:

Beta-actin forward 5′-CACTGAGGCTCCCCTGAATCCC-3′.
Beta-actin reverse 5′-CGTACAGAGAGAGCACAGCCTGG-3′.
wasla forward 5′-CAAATGTGGGCTCTCTCCTTCTGAC-3′.
wasla reverse 5′-GAGGGTTGTCTTTCACCAAACAGGC-3′.

Melting curve analysis was used to ensure primer specificity. For qPCR analysis, the threshold cycle (Ct) values for each gene were normalized to expression levels of ß-actin and relative quantification of gene expression determined with the comparative Ct (ΔΔCt) method using the LightCycler® 96 Software (Roche).

2.12 | Survival assay

HRasV12^{-}, HRasV12^{+} and HRasV12^{+}; wasla larvae were screened at 2 dpf for positive transgene expression then were housed in a

purpose-built zebrafish facility, in the Queen's Medical Research Institute, maintained by the University of Edinburgh Biological Resources. Larvae were kept by 20 per nursing tanks (three replicates) at 28°C on a 14 h light/10 h dark photoperiod, daily fed by facility's staff members from 5 to 31 dpf. Surviving larvae were counted every day for 1 mpf.

2.13 | Statistical analysis

All experiments were performed in replicates. Within the figure, legends "N" indicates the number of replicates while "n" indicates the total number of larval fish analysed. All measured data were analysed using StatPlus (AnalystSoft, Inc.). Unpaired two-tailed Student's *t*-tests were performed to compare two experimental groups, and one-way ANOVA with Bonferroni's post-hoc tests for comparisons between multiple experimental groups. Statistical values of $p < .05$ were considered to be significant. All graphs were plotted in Prism 8 (GraphPad Software) and values presented as population means ± *SD*.

3 | RESULTS

3.1 | Pre-neoplastic cells affect the microglia population in the larval zebrafish brain

Although an amoeboid morphology is a consistent feature of microglia within gliomas and has been described across models and species (Chia et al., 2018; Hutter et al., 2019; Kvisten et al., 2019; Ricard et al., 2016), the underlying causes and the timing of the change in morphology are not understood.

Here, we investigated the effect of pre-neoplastic cells on the microglia population using a zebrafish GBM model (Mayrhofer et al., 2017). This model is based on overexpression of human HRasV12 in the proliferating regions of the developing central nervous system (CNS) and results in aggressive tumors resembling human mesenchymal GBM (Mayrhofer et al., 2017). To analyse pre-neoplastic stages, we outcrossed the driver fish line *Et(zic4:GAL4TA4,-UAS:mCherry)$_{hmz5}$* (Distel et al., 2009) to the line *Tg(UAS:eGFP-HRasV12)$_{io006}$* (Santoriello et al., 2010; hereafter Zic/HRasV12 model; Figure 1a). The Zic4 enhancer drives Gal4 expression in the proliferating regions of the developing CNS and upon binding of Gal4 to its target UAS sequence, activates expression of mCherry in control larvae (hereafter HRasV12^{-}) and additional eGFP-HRasV12 expression in tumor developing fish (hereafter HRasV12^{+} larvae). In this model, HRasV12 expression is enriched in the telencephalon from 1 day post fertilization (dpf) onwards, followed by the tectal proliferation zone (TPZ) at 2 dpf and in the cerebellum from 3 dpf. The expression is low in the optic tectum (Figure 1a). This set up results in significantly increased proliferation and measurements based on the mCherry signal that is present in HRasV12^{-} and HRasV12^{+} brains revealed an increased brain size in HRasV12^{+} larvae from 3 dpf onwards (Mayrhofer et al., 2017). Our own brain volume measurements confirmed this, and we observed a significant increase of the larval brain volume at 5 dpf in HRasV12^{+} brains (5.4 ± 0.8 10^6 μm^3) compared to HRasV12^{-} brains (2.7 ± 0.3 10^6 μm^3; $p < .0001$; Figure 1b).

To visualize microglia, we performed immunohistochemistry using the microglia specific zebrafish 4C4 antibody in HRasV12^{-} (control) and HRasV12^{+} larvae (Becker & Becker, 2001; Chia et al., 2018; Mazzolini et al., 2019; Tsarouchas et al., 2018). In line with normal zebrafish development, we did not detect microglia progenitor cells in the brain at 1 and 2 dpf (data not shown), whereas they appear within the tectum by 3 dpf, then spread to the entire brain during development in both conditions (Figure 1c). Under normal physiological conditions, mature microglia are highly ramified and are constantly scanning their microenvironment (Nimmerjahn et al., 2005). Once microglia detect changes, such as microenvironment modifications in brain pathologies, they retract their processes and adopt an amoeboid morphology (Karperien, 2013). During zebrafish development microglia show an amoeboid phenotype during brain colonization stages at 3 dpf and transit toward a ramified phenotype over the next two days of development (Mazzolini et al., 2019; Svahn et al., 2013; Figure 1c). In order to test if the exposure to pre-neoplastic cells has an impact on this process, we analysed microglia morphology in HRasV12^{+} larvae at 3 dpf and upon exposure to HRasV12^{+} cells for 2 days (5 dpf). To assess microglial morphology, we used our previously described method to calculate the ratio of the microglia cell surface to microglia cell volume, which can be used as a read out for their morphological changes (Chia et al., 2018; Figure 1d). Within 3 dpf HRasV12^{-} and HRasV12^{+} brains, microglia were mostly amoeboid in both conditions with a percentage of 80% ± 4 and 84% ± 5, respectively (Figure S1A). However, in 5 dpf larvae we detected 67 ± 16% of amoeboid microglia in presence of HRasV12^{+} cells compared to 17 ± 12% in the HRasV12^{-} condition ($p < .0001$; Figure 1d). We previously reported an amoeboid microglial morphology in the presence of pre-neoplastic myrAKT1 neural cells in larval zebrafish brains (Chia et al., 2018). To test if different oncogenes have the same impact on microglial morphology when overexpressed in the same cell type, we decided to overexpress myrAKT1 as well as BRAF-V600E under control of the zic4 promoter. To achieve this, we used the *Et(zic4:GAL4TA4,UAS:mCherry)$_{hmz5}$* driver line and injected UAS:myrAKT1:UAS:BFP as well as UAS:BRAF-V600E plasmids into one cell stage embryos and analysed microglia morphology at 5 dpf. These experiments revealed that both, overexpression of myrAKT1 and BRAFV-600E, induced an amoeboid morphology in microglia comparable to the overexpression of HRASV12 (Figure S1C,D). These results show that the presence of pre-neoplastic cells, independent of oncogene and cell type, affects the establishment of microglia ramification and confers them with an amoeboid phenotype.

Microglia numbers have been shown to be increased in late stage tumors but also during tumor initiation (Badie & Schartner, 2001; Bowman et al., 2016; Chen et al., 2012; Chia et al., 2018; Coniglio & Segall, 2013; Graeber et al., 2002; Li & Graeber, 2012). To test whether the expression of HRasV12 in the developing CNS induces an increase in microglial numbers, we quantified 4C4^{+} cells (microglia) within 3 and 5 dpf brains of control and HRasV12^{+} larvae.

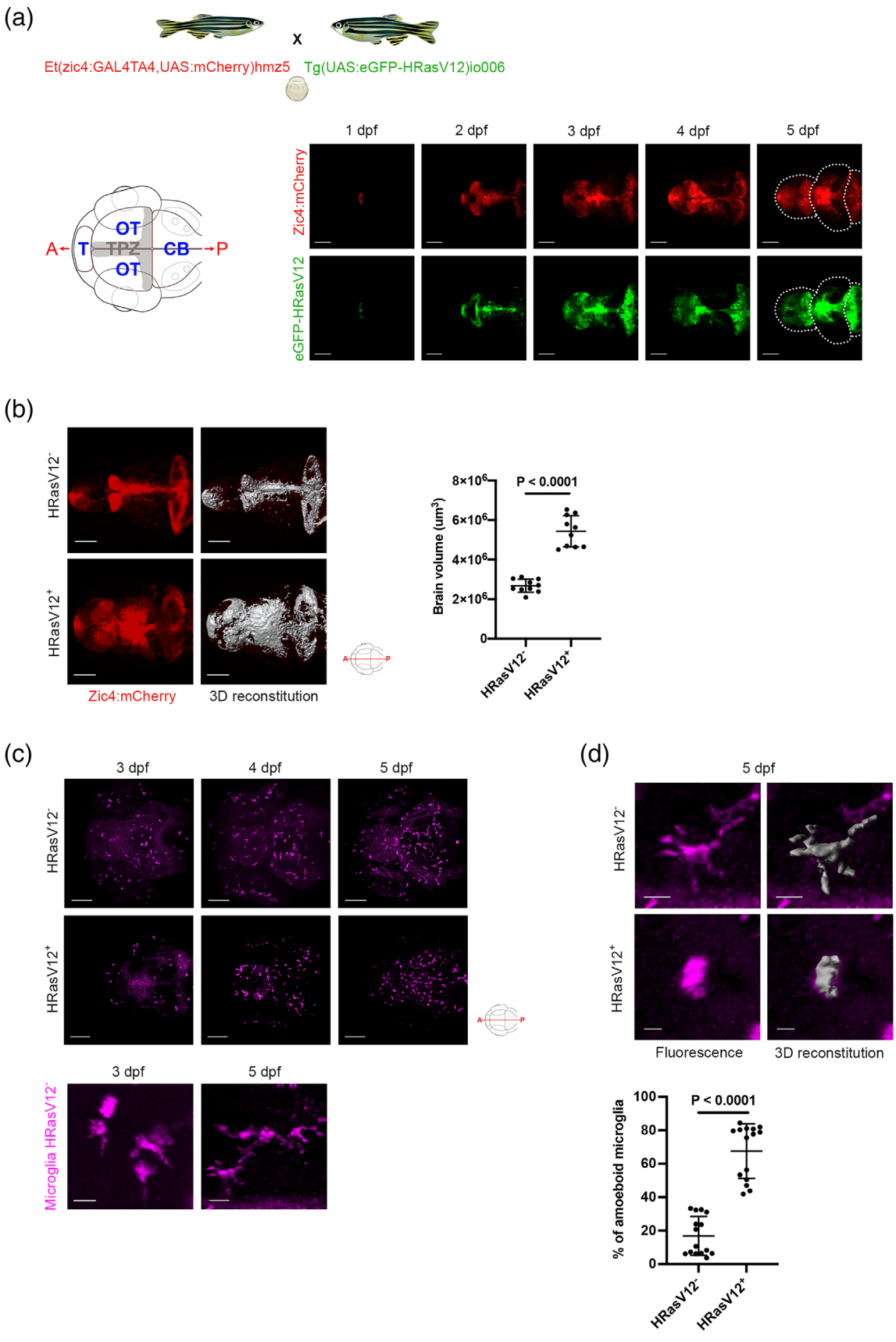

FIGURE 1 Legend on next page.

Interestingly, while microglial numbers were similar in both conditions at 3 dpf,103 ± 19 and 93 ± 19 microglia respectively (Figure S1B), we detected a significant increase in microglial numbers in HRasV12$^+$ brains at 5 dpf with 198 ± 34 microglia compared to 129 ± 20 microglia in control brains ($p < .0001$; Figure 2a). Interestingly, neither overexpression of myrAKT1 nor overexpression of BRAF-V600E resulted in increased microglia numbers (Figure S1C,D).

To test whether HRasV12$^+$ leads to additional infiltration of macrophages, we used an outcross between *Tg(zic4:Gal4UAS:mCherry:mpeg1:eGFP)* and *Tg(UAS:TagBFP2-HRasV12)* fish lines, and control larvae from the incross between *Tg(zic4:Gal4UAS:mCherry:mpeg1:eGFP)*. The expression of eGFP under the mpeg1 promoter allows to visualize all macrophages including microglia (Ellett et al., 2011) and additional staining using the 4C4 antibody allows to distinguish microglia from macrophages. These experiments revealed that in control brains 97% of the myeloid cell population were microglia and this did not change significantly in HRasV12$^+$ brains (Figure S1E). Hence, pre-neoplastic HRasV12$^+$ cells do not lead to the infiltration of macrophages.

To understand how the increase of the microglia population is achieved, we assessed microglial proliferation activity by performing an EdU assay, and stained control and HRasV12$^+$ larval microglia (4C4$^+$). The number of EdU$^+$/4C4$^+$ cells was significantly higher in HRasV12$^+$ brains (21 ± 19 %) compared to control brains (2 ± 2%; $p = .0003$; Figure 2b). Thus, the exposure of microglia to pre-neoplastic HRasV12$^+$ cells from 3 to 5 dpf triggers their proliferation and results in a significant increase of their number.

Taken together, our results show that microglia number and morphology are not affected by the immediate presence of pre-neoplastic cells, however within 2 days, microglia numbers increased significantly, and showed a higher percentage of amoeboid cells compared to controls.

3.2 | Pre-neoplastic HRasV12$^+$ cells affect microglial functions

In light of our previous observations on amoeboid microglial morphology, we decided to investigate effects of HRasV12$^+$ cells on fundamental microglial functions such as phagocytosis and motility. The clearance of dying cells and debris in the brain is carried out by microglia and their aptitude to respond to lesions is well described in the literature (Ayata et al., 2018; Davalos et al., 2005; Neumann et al., 2008; Nimmerjahn et al., 2005; Norris et al., 2018; Peri & Nüsslein-Volhard, 2008; Sieger et al., 2012). To measure effects on microglial phagocytic activity, we developed a phagocytosis assay based on zymosan injection (Figure 3a). Zymosan is a yeast cell wall well described to trigger macrophage phagocytosis involving CR3, Mannose, Dectin-1 and Toll-like receptors (Bruggen et al., 2009; Cabec et al., 2000; Mazzolini et al., 2010; Underhill & Ozinsky, 2002). We injected zymosan coupled with a fluorochrome into either the telencephalon or tectum of 5 dpf control and HRasV12$^+$ larval brains, whereas 3 dpf larval brains were only injected into the tectum as very few microglia are detected in the telencephalon at that developmental stage (Figure 1c). Upon zymosan injection, larvae were incubated for 6 h, followed by fixation and staining for microglia using the 4C4 antibody (Figure 3a). This assay allowed us to quantify the percentage of phagocytosed zymosan by microglia in HRasV12$^-$ and HRasV12$^+$ brains to determine whether pre-neoplastic cells affect their phagocytic activity (Figure 3a). The percentage of phagocytosis was not significantly different in the tectum of 3 dpf control (19 ± 22%) and HRasV12$^+$ larvae (14 ± 12%), whereas phagocytosis was significantly reduced in 5 dpf HRasV12$^+$ larvae (tectum: 16 ± 20%; telencephalon: 15 ± 19%) compared to control larvae (tectum: 31 ± 21%; telencephalon: 41 ± 22%; $P_{tectum} = 0.0074$; $P_{telencephalon} = 0.0023$; Figure 3b). These results indicate that within 2 days of contact with pre-neoplastic cells, microglia exhibit a strong reduction of their phagocytic activity.

During early stages of brain development, microglia are very efficient at clearing debris and apoptotic cells due to their high motility (Haynes et al., 2006; Kyrargyri et al., 2020; Madry, Kyrargyri, et al., 2018; Sieger et al., 2012). To assess if the observed change in microglial morphology/function in HRasV12$^+$ larvae has an impact on their motility, we performed high resolution confocal live imaging on HRasV12$^+$ larvae from the outcross between *Tg(zic4:Gal4UAS:mCherry:mpeg1:eGFP)* and *Tg(UAS:TagBFP2-HRasV12)*

FIGURE 1 HRasV12 expression in the proliferating regions of the developing CNS alters microglia morphology. (a) Schematic representation of the zebrafish germline system used to induce HRasV12 expression based on the outcross of the indicated fish lines. Schematic anterior-posterior dorsal view of the brain representing the main sub-divisions: telencephalon (T), optic tectum (OT) cerebellum (CB) and tectal proliferation zone (TPZ) in gray. Confocal images showing mCherry and eGFP-HRasV12 fluorescent signal in the proliferating regions of the developing brain of HRasV12$^+$ larvae from 1 to 5 dpf. White dotted lines mark the main brain subdivisions. Scale bar represents 100 μm. (b) Brain volume was assessed using Imaris surface tool to build the segmented images (right panels) of the mCherry signal (left panels) of proliferating regions of the developing brain from 5 dpf HRasV12$^-$ (top panels) and HRasV12$^+$ (bottom panels). Scale bar represents 100 μm. Brain volumes of 5 dpf HRasV12$^-$ and HRasV12$^+$ larvae were quantified. HRasV12$^-$: $n = 10$; HRasV12$^+$: $n = 10$; $N = 3$. (c) Confocal images of microglia (magenta) distribution throughout the developing brain of HRasV12$^-$ (top panels) and HRasV12$^+$ brains (bottom panels) from 3 to 5 dpf, using 4C4 antibody to specifically label microglia. Scale bar represents 100 μm. Close-ups of microglia at 3 dpf and 5 dpf under physiological condition (HRasV12$^-$) allow to determine their morphology: amoeboid and ramified. Scale bar represents 10 μm. (d) Close-ups of microglia from 5 dpf HRasV12$^-$ (top panels) and HRasV12$^+$ (bottom panels) larvae (left panels) and their segmented images in 3D (right panels) using Imaris surface tool, to assess microglia morphology. Scale bar represents 10 μm. The number of amoeboid microglia was quantified within the microglial population of 5 dpf control and HRasV12$^+$ larvae. Results are shown as a percentage of total microglia. HRasV12$^-$: $n = 15$; HRasV12$^+$: $n = 15$; $N = 3$. Error bars represent mean ± *SD*. Images were captured using a Zeiss LSM710 confocal microscope with a 20X/NA 0.8 objective. All images represent the maximum intensity projections of Z stacks

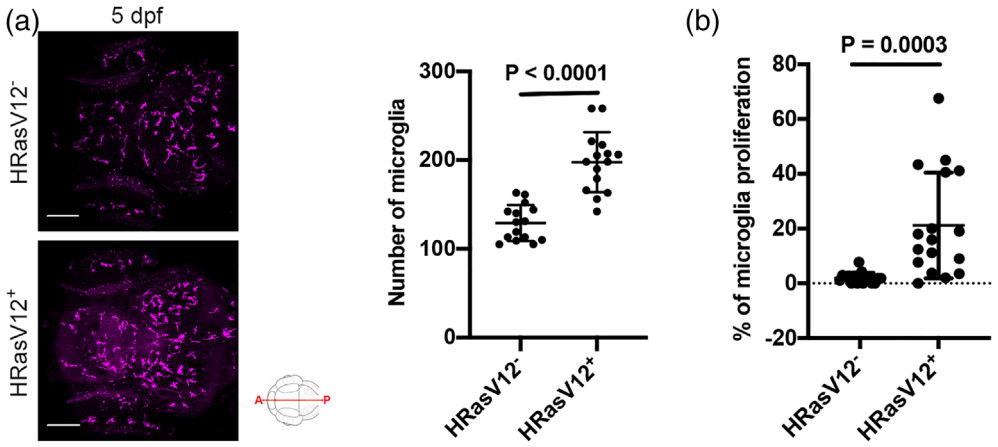

FIGURE 2 Pre-neoplastic cells promote microglia proliferation. (a) Confocal images of the microglial population (magenta) of 5 dpf HRasV12^{-} (top panel) and HRasV12^{+} (lower panel) larvae. Scale bar represents 100 μm. Quantifications revealed a higher number of microglia in HRasV12^{+} brains compared to HRasV12^{-} brains at 5 dpf. HRasV12^{-}: $n = 15$; HRasV12^{+}: $n = 15$; $N = 3$. Error bars represent mean ± *SD*. (b) To measure microglia proliferation, the number of 4C4^{+}/EdU^{+} cells was measured within the microglial population of 5 dpf control and HRasV12^{+} larvae. Results are expressed as a percentage of total microglia. HRasV12^{-}: $n = 17$; HRasV12^{+}: $n = 17$; $N = 3$. Error bars represent mean ± *SD*. Error bars represent mean ± *SD*. Images were captured using a Zeiss LSM710 confocal microscope with a 20X/NA 0.8 objective. All images represent the maximum intensity projections of Z stacks

fish lines, and control larvae from the incross between *Tg(zic4:Gal4-UAS:mCherry:mpeg1:eGFP)*. Based on our previous observations on microglia morphology, number and phagocytosis, we decided to perform confocal live imaging for 13 h on larvae between 3 and 4 dpf and between 4 and 5 dpf. We tracked microglial movement in three-dimensional (3D) for the full duration of the time series and calculated the track length (motility) and their speed of movement in the two different conditions. Interestingly, in presence of HRasV12^{+} cells at 3 dpf, microglia speed (0.007 ± 0.002 μm/s) and motility (312 ± 165 μm) were similar to control microglia speed (0.007 ± 0.004 μm/s) and motility (335 ± 103 μm; Figure 3c). However, we observed an obvious reduction of microglia motility in presence of pre-neoplastic cells at 5 dpf compared to controls (Figure 3d). Quantification of microglial speed (0.009 ± 0.003 μm/s) and motility (425 ± 144 μm) in HRasV12^{+} larvae compared to speed (0.012 ± 0.003 μm/s) and motility of microglia in HRasV12^{-} larvae (567 ± 173 μm) showed a significant difference ($P_{speed} = 0.001$; $P_{motility} = 0.001$; Figure 3d).

In summary, our results show that within a short time window, pre-neoplastic cells alter not only microglial morphology but also key functions such as phagocytosis and motility at early stages of GBM formation. Hence, we speculated that lasting alterations of the microglial actin cytoskeleton might be the underlying cause, which result in a permanent change in morphology and impair related functions such as motility and phagocytosis.

3.3 | RNA sequencing of isolated microglia reveals down-regulation of *wasla* gene expression

Our data show that microglia morphology, phagocytosis and motility are altered upon contact with pre-neoplastic cells. These cellular mechanisms are regulated by a compilation of different signaling pathways, but they are all orchestrated by the actin cytoskeleton organization (Freeman & Grinstein, 2014; Pollard & Cooper, 2009; Svitkina, 2018). Hence, we decided to conduct RNA sequencing to investigate differentially expressed (DE) genes involved in actin cytoskeleton organization and regulation between control and HRasV12^{+} conditions at 3 and 5 dpf. Following our previously published protocols, we isolated microglia from dissociated brains, stained them using the 4C4 antibody and sorted using flow cytometry (Mazzolini et al., 2018, 2019; Figure S2). For each time point, microglia were pooled from 600 HRasV12^{-} and HRasV12^{+} larval brains and three replicates were performed per time point for RNA sequencing.

We evaluated the expression correlation between biological replicates using the whole set of genes from the RNA-seq data set. Each sample consisted of isolated microglia from 600 brains; of note, scatter plots of the normalized transformed read counts showed that biological replicates were highly correlated ($r > 0.75$). Interestingly, correlation between control (HRasV12^{-}) samples was higher at 3 dpf ($r > 0.83$) and 5 dpf ($r > 0.81$) than between HRasV12^{+} samples ($r > 0.75$) and ($r > 0.79$; Figure S3A). The lower correlation obtained at 3 and 5 dpf from HRasV12^{+} larval brains could be explained by heterogeneity in those samples due to the presence of pre-neoplastic cells (Figure S3A). PCA confirmed this correlation by showing HRasV12^{-} replicates are more clustered than replicates from HRasV12^{+} conditions. Moreover, clusters corresponding to 3 and 5 dpf samples from both conditions were well segregated (Figure S3B). A global analysis of our data using the KEGG database showed an enrichment for few pathways at 3dpf, whereas we did not detect an enrichment for specific pathways in microglia from HRasV12^{+} brains compared to controls (Table S1). However, we detected 187 differentially expressed (DE) genes

(FDR < 0.05, fold change > |2|) in microglia from HRasV12^{+} brains at 3 dpf and 346 DE genes at 5 dpf (Table S2). As we were speculating that actin cytoskeleton organization is impaired in microglia in HRasV12^{+} brains, we then used KEGG and defined pathways related to actin cytoskeleton in zebrafish (Regulation of actin cytoskeleton, Focal adhesion, Adherens junction, Tight junction and mTOR signaling pathway) and selected genes from our RNA-seq which are referred to them (Table S3). We compared expression of

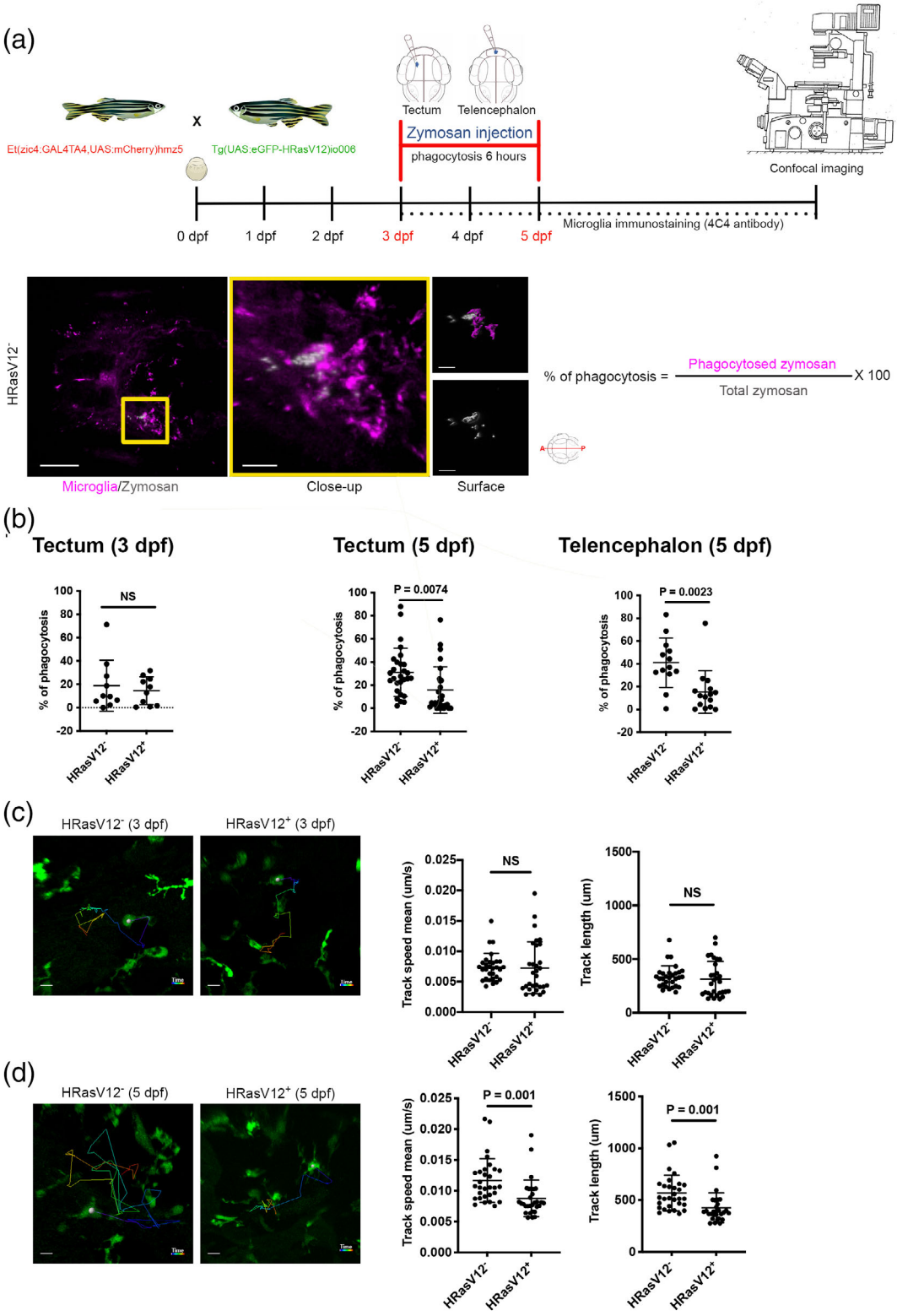

FIGURE 3 Legend on next page.

these genes in microglia between control and HRasV12$^+$ larval brains at 3 and 5 dpf and focussed on genes that are differentially expressed (FDR < 0.05, fold change > |2|) at 5 dpf when pre-neoplastic cells affect microglial functions. We obtained 11 differentially expressed (DE) genes, 8 with lower expression and 3 with higher expression in microglia from HRasV12$^+$ brains compared to control microglia (Figure 4a, Table S3). The majority of these genes belonged to the "Regulation of actin cytoskeleton" pathway, and the identified top ranked DE gene was *wasla* (Table S3), the zebrafish orthologue of human WASP like actin nucleation promoting factor (WASL, also known as N-WASP). WASL is a key protein of the actin cytoskeleton organization, necessary to maintain cell shape, efficient phagocytosis and motility (Dogterom & Koenderink, 2019; May et al., 2000; Niedergang & Grinstein, 2018; Yamaguchi et al., 2005). *Wasla* showed 4.2 times lower expression in microglia in the presence of pre-neoplastic cells compared to microglia from control brains (FDR = 0,005). Intriguingly, *wasla* was the only gene of the WASP family significantly differentially expressed in microglia in the presence of pre-neoplastic cells, whereas *was*, *wasf* and *wash* expressions were the same as in control microglia (Figure 4b).

To test if *WASL* expression is altered in microglia within human gliomas, we accessed RNA sequencing data recently generated by Klemm et al. (2020)). Here, we focussed on *IDH* WT gliomas, which typically represent grade IV glioblastomas and are highly infiltrated by macrophages (MDMs) and microglia. We compared expression levels of *WASL* in MDMs and microglia isolated from these tumors to isolated cells from non-tumor samples. Interestingly, while *WASL* expression was not altered in MDMs ($p = .89$), we detected lower expression levels of this gene in microglia of *IDH* WT gliomas in comparison to microglia from non-tumor samples (Figure 4c). Although not statistically significant, the data shows a clear trend ($p = .14$).

Our results show that microglia exposed to pre-neoplastic cells express a lower level of *wasla*. Thus, we hypothesized that reduced levels of *wasla* are the underlying cause of the change of microglial morphology and the decrease of their motility and phagocytic capacity.

3.4 | Microglia specific overexpression of *wasla* restores microglial functions in HRasV12$^+$ brains

In order to test our hypothesis that lower expression levels of *wasla* were responsible for the observed changes in microglial morphology and functions, we performed cell specific overexpression for *wasla* in microglia. To achieve this, we created a plasmid, which encodes for *wasla* under the control of the mpeg1 promoter specific to microglia and macrophages (Ellett et al., 2011). Injection of the mpeg1:wasla plasmid into one cell stage embryos resulted in a transient, mosaic expression of *wasla* in microglia. To verify the efficiency of this strategy, we injected the plasmid into one cell stage *Tg(mpeg1:mCherry)* embryos, isolated mCherry$^+$ microglia/macrophages at 5 dpf by FACS (Figure S4A) and performed qPCR for *wasla*. We obtained a 1.46 times higher expression of *wasla* in mCherry$^+$ microglia/macrophages from injected embryos compared to non-injected embryos (Figure S4B). Hence, we injected the mpeg1:wasla plasmid into HRasV12$^-$ and HRasV12$^+$ embryos and analysed the impact on microglia at 5 dpf. Injection into HRasV12$^-$ embryos (hereafter HRasV12$^-$; wasla), did not alter microglia morphology (HRasV12$^-$; wasla: 9 ± 4%; HRasV12$^-$: 7 ± 2%) and number (HRasV12$^-$; wasla: 146 ± 17; HRasV12$^-$: 143 ± 16) compared to control larvae (Figure S4C). This shows that higher expression levels of *wasla* do not change microglial appearance under physiological conditions. However, injection of the mpeg1:wasla plasmid into HRasV12$^+$ embryos had a significant impact and restored microglia ramification, number, phagocytic activity and motility in this condition. Upon *wasla* overexpression in microglia of HRasV12$^+$ larvae, the number of amoeboid cells was significantly reduced in HRasV12$^+$; wasla (33 ± 14%) compared to the HRasV12$^+$ condition (67 ± 16%; $p < .0001$) and their morphology similar to control microglia (Figure 5a, top panels; Figure 5b). Furthermore, microglia numbers were significantly reduced compared to the HRasV12$^+$ condition (198 ± 34; $p < .0001$) and were similar to control microglia numbers with 128 ± 32 microglia in HRasV12$^+$; wasla compared to 131 ± 22 in control larvae (Figure 5a, middle panels; Figure 5c). Finally, microglial phagocytic activity (53 ± 32%), speed (0.012 ± 0.003 μm/s) and motility (584 ± 156 μm) in 5 dpf HRasV12$^+$; wasla

FIGURE 3 HRasV12$^+$ cells affect actin cytoskeleton dependent microglial functions. (a) Schematic representation of the phagocytosis assay used to measure microglia phagocytic activity of 3 and 5 dpf HRasV12$^-$ and HRasV12$^+$ larvae. Zymosan coupled with a fluorochrome was injected into either the telencephalon or the tectum of HRasV12$^-$ and HRasV12$^+$ larvae at 3 and 5 dpf. Larvae were incubated for 6 h post-injection at 28.5°C, fixed, then labeled with the 4C4 antibody to visualize microglia. Confocal image of a 5 dpf control larval brain injected with zymosan (white) into tectum (yellow square). Scale bar represents 100 μm. Close-up of the injection site reveals zymosan phagocytosed by microglia (magenta). Scale bar represents 20 μm. The Imaris surface tool was used to segment and read out the sum of fluorescence from zymosan internalized by microglia (magenta surface) as well as the total amount of injected zymosan within the telencephalon or tectum (gray surface). The percentage of phagocytosis was calculated following the indicated formula. (b) Efficiency of phagocytosis was calculated for 3 and 5 dpf HRasV12$^-$ and HRasV12$^+$ larvae injected with zymosan into either the telencephalon or the tectum. Results are expressed as a percentage of the total amount of injected zymosan. 3 dpf: HRasV12$^-$: $n = 10$; HRasV12$^+$: $n = 10$; $N = 3$; 5 dpf (tectum): HRasV12$^-$: $n = 28$; HRasV12$^+$: $n = 28$; $N = 3$; 5 dpf (telencephalon): HRasV12$^-$: $n = 13$; HRasV12$^+$: $n = 13$; $N = 3$; Error bars represent mean ± *SD*. (c,d) Microglia movement in 3D (motility) was tracked using Imaris tracking tool for the full duration of time series (13 h, $\Delta t = 14$ min). Examples of microglia tracks displayed as time color-coded lines from the different conditions. Scale bar represents 20 μm. Track speed mean and track length were calculated in HRasV12$^-$ and HRasV12$^+$ conditions at 3 (c) and 5 dpf (d). 3 dpf: HRasV12$^-$: $n = 30$; HRasV12$^+$: $n = 30$; $N = 3$; 5 dpf: HRasV12$^-$: $n = 30$; HRasV12$^+$ $n = 3$; $N = 3$; Error bars represent mean ± *SD*. Images were captured using a Zeiss LSM880 confocal microscope with a 20X/NA 1.0 objective. All images represent the maximum intensity projections of Z stacks

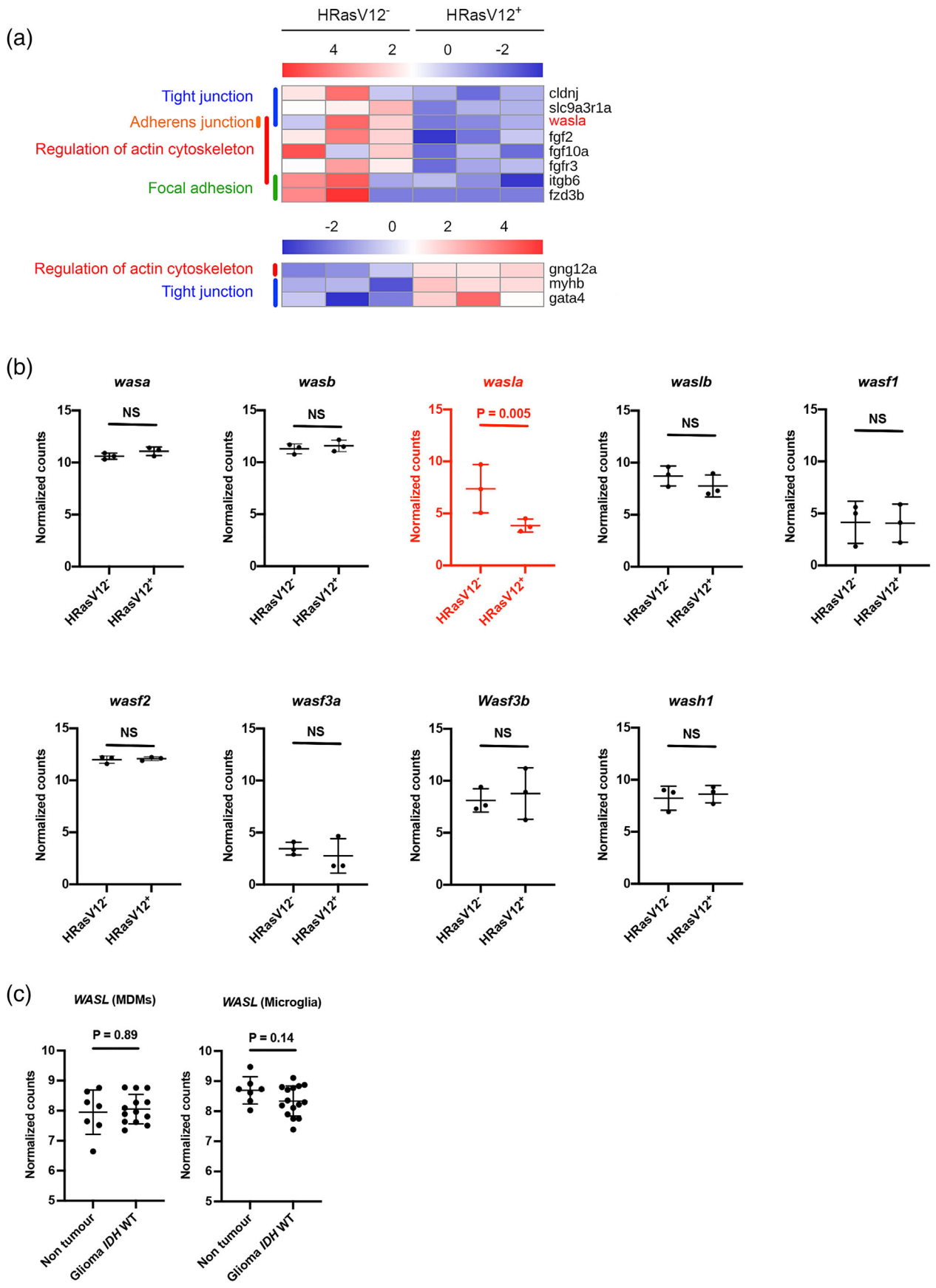

FIGURE 4 Legend on next page.

larvae were significantly different to HRasV12$^+$ larvae (phagocytosis: 16 ± 20%; speed: 0.009 ± 0.003 μm/s; motility: 426 ± 144 μm), and reached same values as control larvae (phagocytosis: 31 ± 21 %; speed: 0.012 ± 0.003 μm/s; motility: 567 ± 173 μm; $P_{phagocytosis} < 0.0001$; $P_{speed} = 0.0005$; $P_{motility} = 0.0006$; Figure 5a, lower panels; Figure 5d).

In summary, these results reveal that *wasla* is a key gene to maintain microglial functions and its lower expression levels in HRasV12$^+$ brains are responsible for alterations in microglia morphology, phagocytosis and motility.

3.5 | Rescue of *wasla* expression in microglia slows down pre-neoplastic growth by restoring an efficient microglial phagocytic activity

Intrigued by the restoration of microglia morphology and functions by *wasla* overexpression in the HRasV12$^+$ condition, we investigated its impact on pre-neoplastic growth and survival of the larval zebrafish. The Zic/HRasV12 model has been previously described with a survival rate of 4% in the first month (Mayrhofer et al., 2017). Therefore, we monitored survival in HRasV12$^-$, HRasV12$^+$ and HRasV12$^+$; wasla conditions daily for 1 month. The survival of HRasV12$^+$ larvae reached 7 ± 6% at 1 month post-fertilization (mpf) compared to 83 ± 16% for controls, which is in line with previously published data (Figure 6a; Mayrhofer et al., 2017). The number of HRasV12$^+$ surviving larvae dropped drastically around 10 dpf, however, HRasV12$^+$; wasla larvae showed better survival during these time points and deteriorated with a significant delay ($p = .0017$; Gehan–Breslow–Wilcoxon test). Finally, HRasV12$^+$; wasla larvae reached a similar survival rate as HRasV12$^+$ larvae (5 ± 5%) at 31 dpf (Figure 6a).

These results show that *wasla* overexpression in microglia improves survival during the initial stages of pre-neoplastic growth in HRasV12$^+$ larvae. Hence, we speculated that tumor formation has been altered in HRasV12$^+$; wasla larvae. To investigate whether *wasla* overexpression in microglia affects pre-neoplastic mass growth (HRasV12$^+$ cells), we measured the brain volume (mCherry signal) and pre-neoplastic mass (eGFP signal) of 5 dpf HRasV12$^+$; wasla brains compared to HRasV12$^+$ and control brains. Interestingly, *wasla* overexpression in microglia significantly reduced the larval brain volume (1.7 ± 0.4 10^6 μm^3; $p = .055$) and pre-neoplastic mass (2.7 ± 0.5 10^6 μm^3; $p = .012$) compared to HRasV12$^+$ brains (2.3 ± 0.5 10^6 μm^3 and 3.6 ± 0.6 10^6 μm^3, respectively). Notably, the HRasV12$^+$; wasla brain volume was reduced to the same volume as that of control brains (1.7 ± 0.3 10^6 μm^3; Figure 6b). These data reveal that the survival improvement of HRasV12$^+$; wasla larvae correlates with a significant reduction of their brain volume and pre-neoplastic mass.

As we have shown that microglial morphology and actin-dependent functions such as phagocytosis were restored in these larvae, we hypothesized that phagocytosis of pre-neoplastic cells by microglia contributed to the reduced pre-neoplastic growth and better survival. To address this hypothesis, we first of all tested the direct impact of rescued *wasla* expression in microglia on phagosome formation. Here, we made use of the *Tg(zic4:Gal4UAS:mCherry:mpeg1:eGFP)* and performed high resolution confocal imaging at 5 dpf. This allowed us to directly observe microglia engulfing mCherry labeled cells. These cells can then be detected within vesicular structures, which are the phagosomes of the microglia (Movie S1; Figure S5, red arrowheads). Of note, not all phagosomes were mCherry positive as microglia also engulfed other cell types that were not labeled with mCherry (Movie S1; Figure S5, yellow arrowheads). These phagosomes simply appear as black holes as the GFP signal within the microglia is restricted to the cytoplasm (Figure S5, yellow arrowheads).

Based on this, we quantified the number of phagosomes per microglia of 5 dpf HRasV12$^+$ and HRasV12$^+$; wasla larval brains from the outcross between *Tg(zic4:Gal4UAS:mCherry:mpeg1:eGFP)* and *Tg(UAS:TagBFP2-HRasV12)* fish lines. If *wasla* was, as we predicted, involved in microglia actin cytoskeleton organization then its overexpression should modify phagosome formation (Marion et al., 2012; May et al., 2000; Niedergang & Grinstein, 2018). Importantly, microglia overexpressing *wasla* in HRasV12$^+$ larvae contained 3 ± 3 phagosomes whereas HRasV12$^+$ microglia contained only 1 ± 1 phagosome ($p < .0001$; Figure 6c). Therefore, these results confirm that rescue of *wasla* expression in microglia of HRasV12$^+$ larvae increases phagosome formation. Hence, we tested if this leads to an increase in phagocytosis of HRasV12$^+$ cells. To investigate the phagocytosis of HRasV12$^+$ cells by microglia, we used the outcross between *Et(zic4:GAL4TA4,UAS:mCherry)$_{hmz5}$* and *Tg(UAS:eGFP-HRasV12)$_{io006}$*. We isolated microglia and performed flow cytometry to quantify the mean of fluorescence from GFP$^+$ (HRasV12$^+$) cells phagocytosed by microglia from HRasV12$^+$ and HRasV12$^+$; wasla larval brains (Table 2). These quantifications revealed that the amount of pre-neoplastic cells engulfed by HRasV12$^+$; wasla microglia was 1.5 higher than in the HRasV12$^+$ condition ($p = .0002$; Figure 6d). Hence, the restoration of phagocytic activity in microglia results in an increased phagocytosis of pre-neoplastic HRasV12$^+$ cells. This might

FIGURE 4 The actin nucleation promoting factor *wasla* is less expressed in microglia from HRasV12$^+$ larvae. (a) Heatmap of differentially expressed (DE) genes (FDR < 0.05, Fold Change > |2|) from microglia transcriptome comparisons between 5 dpf HRasV12$^-$ and HRasV12$^+$ larval brains (11 genes), belonging to zebrafish actin cytoskeleton KEGG pathways [Regulation of actin cytoskeleton, Focal adhesion, Adherens junction, Tight junction and mTOR signaling pathway]. The actin nucleation promoting factor *wasla* is the top ranked gene of the list. See also Table S3. (b) Dot plots of normalized transformed read counts of the representative WASP family genes. Black plots represent non-DE genes whereas, red plots correspond to DE genes at 5 dpf between control and HRasV12$^+$ conditions. (b) The means ± *SD* of three independent experiments are plotted. (c) Dot plots of normalized transformed read counts of *WASL* gene expression of monocyte-derived macrophages (MDMs) and microglia in human non tumor and glioma *IDH* WT brain samples (Klemm et al., 2020)

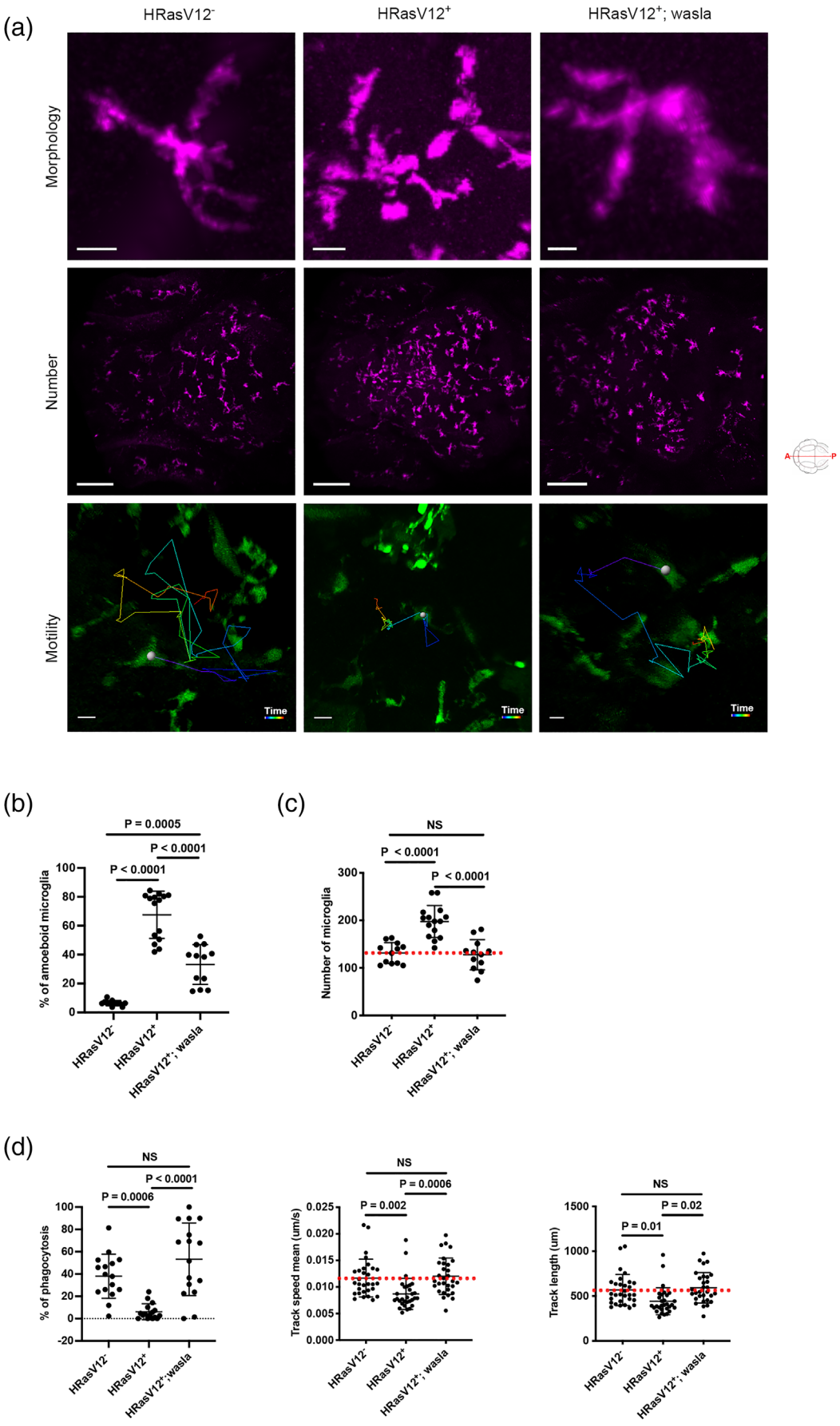

FIGURE 5 Legend on next page.

explain the smaller pre-neoplastic mass volume in HRasV12$^+$; wasla larvae.

4 | DISCUSSION

In this study, we revealed the impact of pre-neoplastic cells on the microglial population, their morphology and functions during tumor initiating stages. Several elegant studies have shown crosstalk between GAMs and neoplastic cells in the brain creating a microenvironment favorable to tumor growth and maintenance (for review see (Gutmann & Kettenmann, 2019). However, while the amoeboid microglial morphology has been described across models and species (Annovazzi et al., 2018; Bayerl et al., 2016; Chia et al., 2018; Juliano et al., 2018; Kvisten et al., 2019; Resende et al., 2016; Ricard et al., 2016), the underlying causes and the timing for the change in morphology are not understood. To our knowledge, this is the first study to provide mechanistic insights of an alteration of microglia morphology and functions due to lower expression levels of the *wasl* gene in presence of tumor initiating cells. We utilized a well-established larval zebrafish brain tumor model to address the earliest stages of tumor induction due to activation of oncogenes. By overexpressing a constitutively active form of the human *HRas* gene, we induced cellular alterations in the larval zebrafish brain that lead to the formation of tumors similar to the mesenchymal subtype of human GBM by 1 month postfertilization (Mayrhofer et al., 2017). Mesenchymal subtype GBMs have been found to correlate with a stronger enrichment of GAMs compared to proneural and classical GBM subtypes (Bhat et al., 2013; Wang et al., 2017). Here, we strategically worked with 3 and 5 dpf larvae to monitor the pre-neoplastic cell impact on microglia. By using immunohistochemistry, transgenic zebrafish lines for microglia, functional assays and in vivo imaging we revealed that increased microglial numbers, morphological changes, reduced motility and phagocytic activity are established at the earliest stages of tumor development. The large number of microglia observed in 5 dpf HRasV12$^+$ larval brains resulted from a strong proliferative activity. Abels et al. showed that glioma cells can reprogramme microglia and promote their proliferation by reducing expression levels of *Btg2* gene (Abels et al., 2019). In our transcriptomic data *Btg2* and other genes mediating cell proliferation were not differentially expressed (not shown), an observation that does not correlate with our EdU results confirming increased proliferation. However, the EdU assay provided a readout of all proliferative microglia between 3 and 5 dpf, whereas transcriptomic data have been obtained from a specific timepoint and could reflect only a small population of microglia proliferating at that time as all microglia are not synchronized. A single cell RNA sequencing approach might be suited to circumvent this limitation. Furthermore, as we analysed the microglia population during development a certain degree of proliferation is present even in control larvae, hence the additional increase caused by HRasV12$^+$ pre-neoplastic cells might not be strong enough to result in significant changes in gene expression. This could explain why we did not detect variation of proliferation gene expression.

Within our transcriptomic data, *wasla* was the top ranked DE gene belonging to the "Regulation of actin cytoskeleton" pathway. WASL is a key protein of the actin cytoskeleton organization and hence expressed in almost every cell type. Nevertheless, differences in expression levels can be observed. In the human and mouse brain, astrocytes and neurons for example show higher expression levels compared to other cells such as microglia and oligodendrocytes (Zhang et al., 2014, 2016). Among myeloid cells in the brain, Wasl can be detected in every subset with varying expression levels (Li et al., 2019). Interestingly, there seems to be controversy on the role of WASL during cell division. Cytokinesis is the final step of cell division taking place at the end of mitosis, this mechanism is characterized by the formation of a contractile actomyosin ring necessary for the separation of the newly forming daughter cells. Wang et al. concluded that WASL has a role in cytokinesis during porcine oocyte maturation (Wang et al., 2020), whereas others consider that mechanism as WASL independent (Bompard et al., 2008; Deschamps et al., 2013; Schwayer et al., 2016). Our data support the hypothesis that WASL is not involved in cell proliferation but is crucial for other microglial functions.

Across species and glioma models, microglia exhibit an amoeboid phenotype. These amoeboid microglia encompass anti- and pro-tumoral microglia and it needs more investigation to determine the correlation between microglia polarization and this specific morphology. Nevertheless, this phenotype is a reliable readout of physiological changes within the brain microenvironment. According to Karperien et al. amoeboid microglia are usually characterized by their high capacity to engulf and migrate (Karperien, 2013). However, our results reveal a reduced motility, speed and phagocytic activity of amoeboid microglia upon exposure to pre-neoplastic cells. Our data is in line with a study by Voisin et al. who have co-cultured human microglia

FIGURE 5 *Walsa* overexpression in microglia restores their morphology and functions. (a) Close-up confocal images of microglia (top panels), microglial population (middle panels) and examples of microglia tracks displayed as time color-coded lines (lower panels) from 5 dpf HRasV12$^-$ (left panel), HRasV12$^+$ (middle panel) and HRasV12$^+$; wasla (right panel) brains. Scale bar represents 10, 100 and 20 μm, respectively. (b) The percentage of amoeboid microglia and (c) the total number of microglia from 5 dpf HRasV12$^-$, HRasV12$^+$ and HRasV12$^+$; wasla brains were quantified. HRasV12$^-$: $n = 15$; HRasV12$^+$: $n = 15$; HRasV12$^+$; wasla: $n = 15$; $N = 3$. Error bars represent mean ± *SD*. (d) The percentage of phagocytosis within the tectum of 5 dpf HRasV12$^-$, HRasV12$^+$ and HRasV12$^+$; wasla as well as microglia track speed mean and track length (motility) were quantified. Phagocytosis: HRasV12$^-$: $n = 16$; HRasV12$^+$: $n = 16$; HRasV12$^+$; wasla: $n = 16$; $N = 3$. Motility: HRasV12$^-$: $n = 30$; HRasV12$^+$: $n = 30$; HRasV12$^+$; wasla: $n = 30$; $N = 3$. Error bars represent mean ± *SD*. Red dotted lines indicate the number of microglia, track speed mean or track length in control condition. Images were captured using a Zeiss LSM880 confocal microscope with a 20X/NA 0.8 objective. All images represent the maximum intensity projections of Z stacks

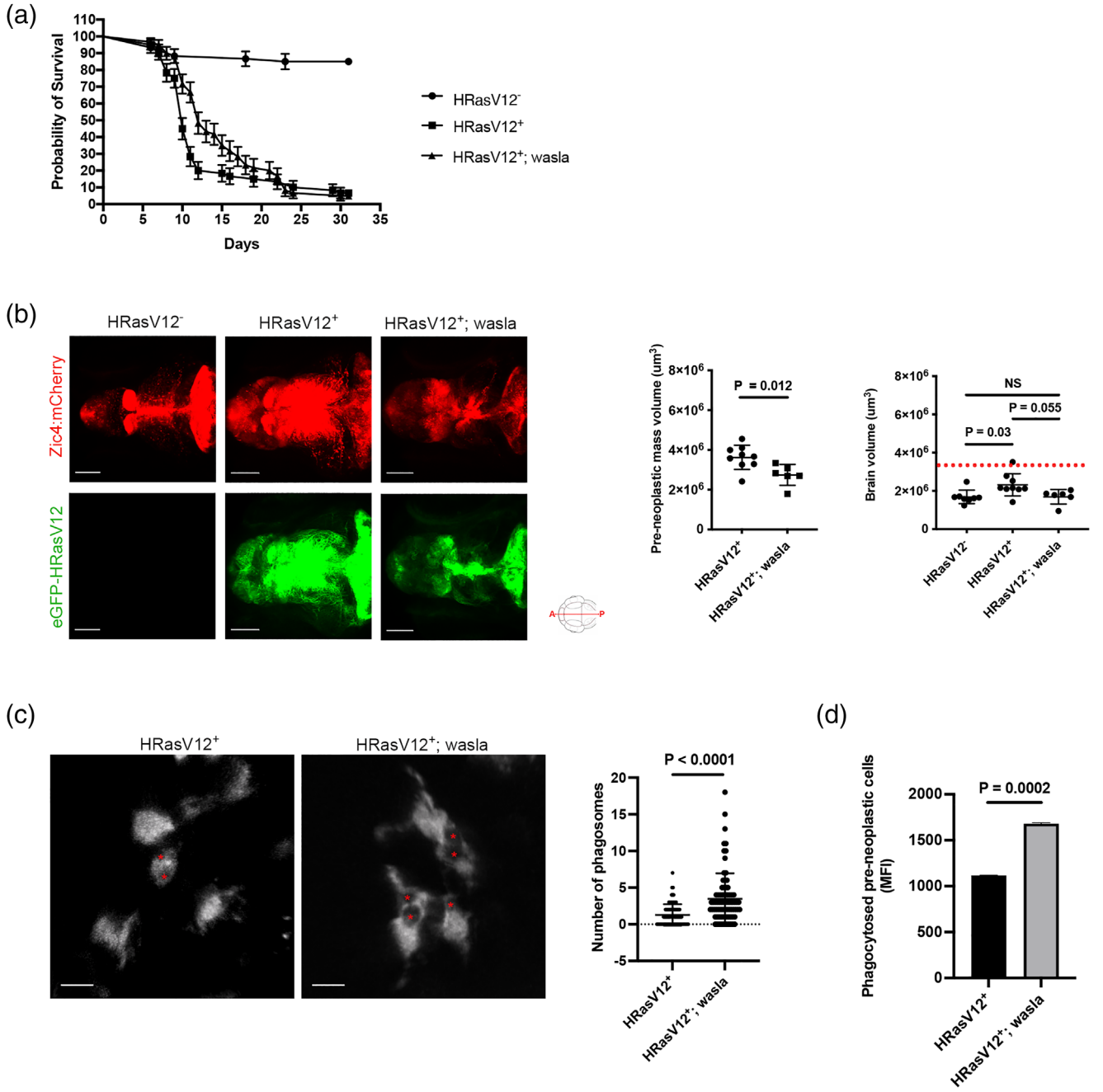

FIGURE 6 Microglial *wasla* expression is crucial to slow down tumor progression. (a) Kaplan–Meier survival plot of HRasV12^{-}, HRasV12^{+} and HRasV12^{+}; wasla larvae control over 31 days, $n = 50/60$, 4/60 and 3/60, respectively. $p = .0017$ (Gehan–Breslow–Wilcoxon test between HRasV12^{+} and HRasV12^{+}; wasla conditions). Error bars represent mean ± *SD*. (b) Brain and pre-neoplastic mass volume were measured using the mCherry signal (brain, top panels) and eGFP signal of HRas^{+} cells (pre-neoplastic mass; bottom panels) of proliferating regions of the developing brain from 5 dpf HRasV12^{-} (left panel), HRasV12^{+} (middle panel) and HRasV12^{+}; wasla (right panel) larvae. Scale bar represents 100 μm. Brain and pre-neoplastic mass volume from 5 dpf HRasV12^{-}, HRasV12^{+} and HRasV12^{+}; wasla larvae are quantified using Imaris surface tool. HRasV12^{+}: $n = 9$; HRasV12^{+}; wasla: $n = 6$; $N = 3$. Error bars represent mean ± *SD*. Red dotted line indicates the brain volume mean in control condition. (c) Close-up confocal images of microglia (mpeg1:eGFP^{+} cells) from 5 dpf HRasV12^{+} (left panel) and HRasV12^{+}; wasla (right panel) brains. Phagosomes are indicated by red asterisks. Scale bar represents 10 μm. The number of phagosomes per microglia from 5 dpf HRasV12^{+} and HRasV12^{+}; wasla brains were quantified. HRasV12^{+}: $n = 80$; HRasV12^{+}; wasla: $n = 80$; $N = 3$. Error bars represent mean ± *SD*. (d) Mean of GFP fluorescent intensity (MFI) from phagocytosed pre-neoplastic cells detected by flow cytometry within isolated microglia from 5 dpf HRasV12^{+} and HRasV12^{+}; wasla larvae. The means ± *SD* of two independent experiments are plotted. Images were captured using a Zeiss LSM880 confocal microscope with a 20X/NA 0.8 objective. All images represent the maximum intensity projections of Z stacks

TABLE 2 Phagocytosis of pre-neoplastic cells by FACS

	Microglia sorting 1		Microglia sorting 2	
	HRasV12+	HRasV12+; Wasla+	HRasV12+	HRasV12+; Wasla+
Number of microglia	3531	2216	3697	2347
GFP (MFI)	1118	1674	1115	1688

cell line (CHME-5) with C6-glioma cells and reported a significant reduction of microglia phagocytic activity after 24 h exposure (Voisin et al., 2010). In HRasV12^{+} larvae, microglia showed alterations of their functions 2 days after exposure to pre-neoplastic cells. Microglial shape, motility and phagocytic activity are actin-dependent and showed dependency on *wasla*. The rescue of *wasla* expression in microglia of HRasV12^{+} brains restored all these physiological functions and promoted phagocytosis of pre-neoplastic cells. The phagocytosis recovery of microglia correlated with a significant diminution of the pre-neoplastic mass volume; hence we concluded that at 5 dpf microglia efficiently clear pre-neoplastic cells and thus limit their growth. The survival curve supports this observation and showed that overexpression of *wasla* in microglia slowed down the deadly effect of tumor growth on larvae from 5 to 20 dpf. These results are promising but further studies are needed to understand the temporary nature of this effect. One explanation might be the transient and mosaic type of expression generated by the injection of *wasla* constructs into oocytes. Here, not all microglia express sufficient levels of *wasla* and expression diminishes over time. A stable transgenic line expressing high levels of *wasla* in all microglia for a prolonged time would be needed to understand if rescued *wasla* expression can maintain phagocytosis of neoplastic cells by microglia in the long run. However, even under these circumstances, phagocytosis might decrease at later stages of tumor growth due to increased expression of "don't eat me" signals such as CD47 by tumor cells (Gholamin et al., 2017; Hutter et al., 2019; Li et al., 2017; Ma et al., 2019).

Of note, isolated microglia from human *IDH* WT gliomas expressed lower levels of *WASL*. Although these results were statistically not significant, they revealed a strong trend ($p = .14$). We speculate that heterogeneity within the microglia population as well as differences in tumor stages might be the underlying explanation. Interestingly, expression levels of *WASL* were not altered in MDMs isolated from human *IDH* WT gliomas. This is in line with previous results on a different impact of the glioma environment on MDMs and microglia and further underpins potential differences in their role within gliomas.

Interestingly, amongst the differentially expressed genes extracted from our transcriptomic data belonging to KEGG pathways linked to "Regulation of actin cytoskeleton" some of the other genes might also contribute to the observed effects. In presence of pre-neoplastic cells microglia expressed lower levels of fibroblast growth factor 2 (fgf2) and fibroblast growth factor receptor 3 (fgfr3), which have been shown to increase microglial migration and phagocytic activity (Noda et al., 2014). Furthermore, *fibroblast growth factor 10a (fgf10a)* showed lower expression in microglia of HRasV12^{+} larvae. FGF10 treatment has been shown to inhibit microglial pro-inflammatory cytokine secretion and proliferation via regulation of the TLR4/NF-$_{K}$B pathway in an animal model after spinal cord injury (Chen et al., 2017). Hence, the reduced expression levels of this gene could contribute to the increased microglial proliferation. Among the DEG that showed higher expression levels in microglia from HRasV12^{+} brains, we detected *G protein subunit gamma 12 (gng12)*. Interestingly, *gng12* is known to be highly expressed after LPS stimulation of microglia and to offset the inflammatory response by reducing levels of nitric oxide and TNFα (Larson et al., 2010). Moreover, long non-coding gng12 RNAs are highly expressed in glioma tissues and its downregulation inhibits proliferation, migration and epithelial-mesenchymal transition of glioma cells (Xiang et al., 2020). These results suggest that high expression levels of *gng12* in microglia exposed to pre-neoplastic cells might contribute to the generation of a pro-tumoral response.

Phagocytic events are associated with cytokine secretion as part of the innate immune response, and in preparation for adaptive immunity (Acharya et al., 2020; Chung et al., 2006; Fu et al., 2014; Heo et al., 2015; Murray et al., 2005). The secretion of cytokines relies on cellular exocytic pathways involving WASL (González-Jamett et al., 2017; Li et al., 2018; Olivares et al., 2014; Ory & Gasman, 2011). Hence, cytokine secretion of microglia might be altered due to the observed low expression levels of *wasla*. Interestingly, microglia isolated from HRasV12^{+} larval brains showed increased expression levels of *il4* and *il11* (not shown), suggesting the generation of an anti-inflammatory state during tumor initiating stages. Therefore, the assessment of microglial cytokine secretion in HRasV12^{+} and HRasV12^{+}; wasla larvae could provide a better understanding of the establishment of an immunosuppressive environment by tumor initiating cells linked to the reduced phagocytic activity of microglia.

To precisely determine the changes in microglial functions in presence of HRasV12^{+} cells, it is important to understand the strategy applied by these cells to alter microglial gene expression levels. Extracellular vesicles (EVs) contain proteins, lipids and different RNA species that change the activity of recipient cells (Tkach & Théry, 2016; Verweij et al., 2019). Several studies have shown the implication of EVs secreted by tumor cells on microglia/macrophages (Abels et al., 2019; Hyenne et al., 2019; Vos et al., 2015). Of note, *wasl* expression has been shown to be regulated by various miRNAs (Bettencourt et al., 2013; Schwickert et al., 2015). Data from the Mione laboratory shows that some of these miRNAs have significantly increased expression levels in HRasV12^{+} cells compared to control cells (Anelli et al., 2018). This includes the miRNA Let-7g-1, which targets the *wasla* gene. Thus, it is tempting to speculate that EVs

secreted by HRasV12^{+} cells transfer miRNAs which mediate changes of microglial gene expression and related functions. Future studies will reveal if Let-7g-1 and other miRNAs transferred to microglia via EVs are the underlying cause of the observed changes.

In conclusion, we show for the first time that during tumor initiation stages, pre-neoplastic cells influence microglial functions by altering their gene expression profiles resulting in an alteration of microglial morphology and related functions. We identify *wasla* as a key component in the regulation of microglial morphology, phagocytosis and migration. Our findings provide a mechanism that empowers pre-neoplastic cells to trap microglia within their vicinity, deactivate their phagocytic functions and promote the generation of an anti-inflammatory tumor promoting microenvironment.

ACKNOWLEDGMENTS

This work was supported by a Cancer Research UK Career Establishment Award to Dirk Sieger (C49916/A17494). The authors thank Dr. Marina Mione for help and discussion on the project, the BRR zebrafish facility (QMRI, The University of Edinburgh) for maintenance and care of the zebrafish, the SURF Biomolecular core, and the QMRI Flow Cytometry and Cell Sorting Facility. Thanks to Prof. Elizabeth Patton and Dr. Zhiqiang Zeng for the plasmid pME-BRAF-V600E (Al-Olabi et al., 2018), to Kest for his work on the graphical abstract (https://www.instagram.com/kest_design/) and to SMART-Servier Medical Art for graphic material that has been slightly modified in part (https://creativecommons.org/licenses/by/3.0/). Thanks to Dr. Katy Marshall-Phelps for proofreading the manuscript.

CONFLICT OF INTEREST

The authors declare no conflict of interest.

AUTHOR CONTRIBUTIONS

Conceptualisation, J.M. and D.S.; Methodology, J.M. and D.S.; Formal Analysis, J.M., S.LC. and C.C.; Investigation, J.M. and G.M.; Resources, D.S. and JF.Z., Data Curation, J.M., S.LC. and C.C.; Writing – Original Draft, J.M. and D.S., Writing - Review & Editing, J.M., S.LC., JF.Z. and DS; Visualisation, J.M. and S.LC.; Supervision, D.S. and JF.Z., Project Administration, J.M. and D.S.; Funding Acquisition, D.S.

DATA AVAILABILITY STATEMENT

The data that support the findings of this study are included in the supplementary tables and are available from the corresponding author upon reasonable request

ORCID

Julie Mazzolini https://orcid.org/0000-0001-9347-5635
Dirk Sieger https://orcid.org/0000-0001-6881-5183

REFERENCES

Abels, E. R., Maas, S. L. N., Nieland, L., Wei, Z., Cheah, P. S., Tai, E., Kolsteeg, C. J., Dusoswa, S.A., Ting, D. T., Hickman, S., El Khoury, J., Krichevsky, A. M., & Breakefield, X. O. (2019). Glioblastoma-associated microglia reprogramming is mediated by functional transfer of extracellular miR-21. *Cell Reports*, *28*(12), 3105–3119.e7. https://doi.org/10.1016/j.celrep.2019.08.036

Acharya, D., Li, X. R. (. L.)., Heineman, R. E.-S., & Harrison, R. E. (2020). Complement receptor-mediated phagocytosis induces proinflammatory cytokine production in murine macrophages. *Frontiers in Immunology*, *10*, 3049. https://doi.org/10.3389/fimmu.2019.03049

Al-Olabi, L., Polubothu, S., Dowsett, K., Andrews, K. A., Stadnik, P., Joseph, A. P., Knox, R., Pittman, A., Clark, G., Baird, W., Bulstrode, N., Glover, M., Gordon, K., Hargrave, D., Huson, S. M., Jacques, T. S., James, G., Kondolf, H., Kangesu, L., & Kinsler, V. A. (2018). Mosaic RAS/MAPK variants cause sporadic vascular malformations which respond to targeted therapy. *The Journal of Clinical Investigation*, *128*(4), 1496–1508. https://doi.org/10.1172/jci98589

Anders, S., Pyl, P. T., & Huber, W. (2015). HTSeq—A Python framework to work with high-throughput sequencing data. *Bioinformatics*, *31*(2), 166–169. https://doi.org/10.1093/bioinformatics/btu638

Andrews, S. (2010). *FastQC: A quality control tool for high throughput sequence data*. Babraham. http://www.bioinformatics.babraham.ac.uk/projects/fastqc

Anelli, V., Ordas, A., Kneitz, S., Sagredo, L. M., Gourain, V., Schartl, M., Meijer, A. H., & Mione, M. (2018). Ras-induced miR-146a and 193a target Jmjd6 to regulate melanoma progression. *Frontiers in Genetics*, *9*, 675. https://doi.org/10.3389/fgene.2018.00675

Annovazzi, L., Mellai, M., Bovio, E., Mazzetti, S., Pollo, B., & Schiffer, D. (2018). Microglia immunophenotyping in gliomas. *Oncology Letters*, *15*(1), 998–1006. https://doi.org/10.3892/ol.2017.7386

Astell, K. R., & Sieger, D. (2017). Chapter 21 Investigating microglia-brain tumor cell interactions in vivo in the larval zebrafish brain. *Methods in Cell Biology*, *138*, 593–626. https://doi.org/10.1016/bs.mcb.2016.10.001

Ayata, P., Badimon, A., Strasburger, H. J., Duff, M. K., Montgomery, S. E., Loh, Y.-H. E., Ebert, A., Pimenova, A. A., Ramirez, B. R., Chan, A. T., Sullivan, J. M., Purushothaman, I., Scarpa, J. R., Goate, A. M., Busslinger, M., Shen, L., Losic, B., & Schaefer, A. (2018). Epigenetic regulation of brain region-specific microglia clearance activity. *Nature Neuroscience*, *21*(8), 1049–1060. https://doi.org/10.1038/s41593-018-0192-3

Badie, B., & Schartner, J. (2001). Role of microglia in glioma biology. *Microscopy Research and Technique*, *54*(2), 106–113. https://doi.org/10.1002/jemt.1125

Bayerl, S. H., Niesner, R., Cseresnyes, Z., Radbruch, H., Pohlan, J., Brandenburg, S., Czabanka, M. A., & Vajkoczy, P. (2016). Time lapse in vivo microscopy reveals distinct dynamics of microglia-tumor environment interactions: A new role for the tumor perivascular space as highway for trafficking microglia. *Glia*, *64*(7), 1210–1226. https://doi.org/10.1002/glia.22994

Becker, T., & Becker, C. G. (2001). Regenerating descending axons preferentially reroute to the gray matter in the presence of a general macrophage/microglial reaction caudal to a spinal transection in adult zebrafish. *The Journal of Comparative Neurology*, *433*(1), 131–147. https://doi.org/10.1002/cne.1131

Bernier, L.-P., Bohlen, C. J., York, E. M., Choi, H. B., Kamyabi, A., Dissing-Olesen, L., Hefendehl, J. K., Collins, H. Y., Stevens, B., Barres, B. A., & MacVicar, B. A. (2019). Nanoscale surveillance of the brain by microglia via cAMP-regulated filopodia. *Cell Reports*, *27*(10), 2895–2908.e4. https://doi.org/10.1016/j.celrep.2019.05.010

Bettencourt, P., Marion, S., Pires, D., Santos, L. F., Lastrucci, C., Carmo, N., Blake, J., Benes, V., Griffiths, G., Neyrolles, O., Lugo-Villarino, G., & Anes, E. (2013). Actin-binding protein regulation by microRNAs as a novel microbial strategy to modulate phagocytosis by host cells: the case of N-Wasp and miR-142-3p. *Frontiers in Cellular and Infection Microbiology*, *3*, 19. https://doi.org/10.3389/fcimb.2013.00019

Bhat, K. P. L., Balasubramaniyan, V., Vaillant, B., Ezhilarasan, R., Hummelink, K., Hollingsworth, F., Wani, K., Heathcock, L., James, J. D.,

Goodman, L. D., Conroy, S., Long, L., Lelic, N., Wang, S., Gumin, J., Raj, D., Kodama, Y., Raghunathan, A., Olar, A., … Aldape, K. (2013). Mesenchymal differentiation mediated by NF-κB promotes radiation resistance in glioblastoma. *Cancer Cell*, *24*(3), 331–346. https://doi.org/10.1016/j.ccr.2013.08.001

Bolasco, G., Weinhard, L., Boissonnet, T., Neujahr, R., & Gross, C. T. (2018). Three-dimensional nanostructure of an intact microglia cell. *Frontiers in Neuroanatomy*, *12*, 105. https://doi.org/10.3389/fnana.2018.00105

Bolger, A. M., Lohse, M., & Usadel, B. (2014). Trimmomatic: A flexible trimmer for Illumina sequence data. *Bioinformatics*, *30*(15), 2114–2120. https://doi.org/10.1093/bioinformatics/btu170

Bompard, G., Rabeharivelo, G., & Morin, N. (2008). Inhibition of cytokinesis by wiskostatin does not rely on N-WASP/Arp2/3 complex pathway. *BMC Cell Biology*, *9*(1), 42. https://doi.org/10.1186/1471-2121-9-42

Bowman, R. L., Klemm, F., Akkari, L., Pyonteck, S. M., Sevenich, L., Quail, D. F., Dhara, S., Simpson, K., Gardner, E. E., Iacobuzio-Donahue, C. A., Brennan, C. W., Tabar, V., Gutin, P. H., & Joyce, J. A. (2016). Macrophage ontogeny underlies differences in tumor-specific education in brain malignancies. *Cell Reports*, *17*(9), 2445–2459. https://doi.org/10.1016/j.celrep.2016.10.052

Bruggen, R. v., Drewniak, A., Jansen, M., Houdt, M. v., Roos, D., Chapel, H., Verhoeven, A. J., & Kuijpers, T. W. (2009). Complement receptor 3, not Dectin-1, is the major receptor on human neutrophils for β-glucan-bearing particles. *Molecular Immunology*, *47*(2–3), 575–581. https://doi.org/10.1016/j.molimm.2009.09.018

Cabec, V. L., Cols, C., & Maridonneau-Parini, I. (2000). Nonopsonic phagocytosis of Zymosan and Mycobacterium kansasii by CR3 (CD11b/CD18) Involves distinct molecular determinants and is or is not coupled with NADPH oxidase activation. *Infection and Immunity*, *68*(8), 4736–4745. https://doi.org/10.1128/iai.68.8.4736-4745.2000

Chen, J., McKay, R. M., & Parada, L. F. (2012). Malignant glioma: Lessons from genomics, mouse models, and stem cells. *Cell*, *149*(1), 36–47. https://doi.org/10.1016/j.cell.2012.03.009

Chen, J., Wang, Z., Zheng, Z., Chen, Y., Khor, S., Shi, K., He, Z., Wang, Q., Zhao, Y., Zhang, H., Li, X., Li, J., Yin, J., Wang, X., & Xiao, J. (2017). Neuron and microglia/macrophage-derived FGF10 activate neuronal FGFR2/PI3K/Akt signaling and inhibit microglia/macrophages TLR4/NF-κB-dependent neuroinflammation to improve functional recovery after spinal cord injury. *Cell Death & Disease*, *8*(10), e3090–e3090. https://doi.org/10.1038/cddis.2017.490

Chia, K., Mazzolini, J., Mione, M., & Sieger, D. (2018). Tumor initiating cells induce Cxcr4-mediated infiltration of pro-tumoral macrophages into the brain. *ELife*, *7*, e31918. https://doi.org/10.7554/elife.31918

Chung, E. Y., Kim, S. J., & Ma, X. J. (2006). Regulation of cytokine production during phagocytosis of apoptotic cells. *Cell Research*, *16*(2), 154–161. https://doi.org/10.1038/sj.cr.7310021

Coniglio, S. J., & Segall, J. E. (2013). Review: Molecular mechanism of microglia stimulated glioblastoma invasion. *Matrix Biology*, *32*(7–8), 372–380. https://doi.org/10.1016/j.matbio.2013.07.008

Costa, A. D. A., Chatterjee, J., Cobb, O., Sanapala, S., Scheaffer, S., Guo, X., Dahiya, S., & Gutmann, D. H. (2021). RNA sequence analysis reveals ITGAL/CD11A as a stromal regulator of murine low-grade glioma growth. *Neuro-Oncology*, *24*(1), 14–16. https://doi.org/10.1093/neuonc/noab130

Daginakatte, G. C., Gianino, S. M., Zhao, N. W., Parsadanian, A. S., & Gutmann, D. H. (2008). Increased c-Jun-NH2-kinase signaling in neurofibromatosis-1 heterozygous microglia drives microglia activation and promotes optic glioma proliferation. *Cancer Research*, *68*(24), 10358–10366. https://doi.org/10.1158/0008-5472.can-08-2506

Daginakatte, G. C., & Gutmann, D. H. (2007). Neurofibromatosis-1 (Nf1) heterozygous brain microglia elaborate paracrine factors that promote Nf1-deficient astrocyte and glioma growth. *Human Molecular Genetics*, *16*(9), 1098–1112. https://doi.org/10.1093/hmg/ddm059

Dart, A. E., Donnelly, S. K., Holden, D. W., Way, M., & Caron, E. (2012). Nck and Cdc42 co-operate to recruit N-WASP to promote FcγR-mediated phagocytosis. *Journal of Cell Science*, *125*(12), 2825–2830. https://doi.org/10.1242/jcs.106583

Davalos, D., Grutzendler, J., Yang, G., Kim, J. V., Zuo, Y., Jung, S., Littman, D. R., Dustin, M. L., & Gan, W.-B. (2005). ATP mediates rapid microglial response to local brain injury in vivo. *Nature Neuroscience*, *8*(6), 752–758. https://doi.org/10.1038/nn1472

Deschamps, C., Echard, A., & Niedergang, F. (2013). Phagocytosis and cytokinesis: do cells use common tools to cut and to eat? Highlights on common themes and differences. *Traffic (Copenhagen, Denmark)*, *14*(4), 355–364. https://doi.org/10.1111/tra.12045

Distel, M., Wullimann, M. F., & Köster, R. W. (2009). Optimized Gal4 genetics for permanent gene expression mapping in zebrafish. *Proceedings of the National Academy of Sciences of the United States of America*, *106*(32), 13365–13370. https://doi.org/10.1073/pnas.0903060106

Dobin, A., Davis, C. A., Schlesinger, F., Drenkow, J., Zaleski, C., Jha, S., Batut, P., Chaisson, M., & Gingeras, T. R. (2013). STAR: Ultrafast universal RNA-seq aligner. *Bioinformatics*, *29*(1), 15–21. https://doi.org/10.1093/bioinformatics/bts635

Dogterom, M., & Koenderink, G. H. (2019). Actin–microtubule crosstalk in cell biology. *Nature Reviews Molecular Cell Biology*, *20*(1), 38–54. https://doi.org/10.1038/s41580-018-0067-1

Ellert-Miklaszewska, A., Dabrowski, M., Lipko, M., Sliwa, M., Maleszewska, M., & Kaminska, B. (2013). Molecular definition of the pro-tumorigenic phenotype of glioma-activated microglia. *Glia*, *61*(7), 1178–1190. https://doi.org/10.1002/glia.22510

Ellett, F., Pase, L., Hayman, J. W., Andrianopoulos, A., & Lieschke, G. J. (2011). mpeg1 promoter transgenes direct macrophage-lineage expression in zebrafish. *Blood*, *117*(4), e49–e56. https://doi.org/10.1182/blood-2010-10-314120

Freeman, S. A., & Grinstein, S. (2014). Phagocytosis: Receptors, signal integration, and the cytoskeleton. *Immunological Reviews*, *262*(1), 193–215. https://doi.org/10.1111/imr.12212

Fu, R., Shen, Q., Xu, P., Luo, J. J., & Tang, Y. (2014). Phagocytosis of microglia in the central nervous system diseases. *Molecular Neurobiology*, *49*(3), 1422–1434. https://doi.org/10.1007/s12035-013-8620-6

Gholamin, S., Mitra, S. S., Feroze, A. H., Liu, J., Kahn, S. A., Zhang, M., Esparza, R., Richard, C., Ramaswamy, V., Remke, M., Volkmer, A. K., Willingham, S., Ponnuswami, A., McCarty, A., Lovelace, P., Storm, T. A., Schubert, S., Hutter, G., Narayanan, C., … Cheshier, S. H. (2017). Disrupting the CD47-SIRPα anti-phagocytic axis by a humanized anti-CD47 antibody is an efficacious treatment for malignant pediatric brain tumors. *Science Translational Medicine*, *9*(381), eaaf2968. https://doi.org/10.1126/scitranslmed.aaf2968

González-Jamett, A. M., Guerra, M. J., Olivares, M. J., Haro-Acuña, V., Baéz-Matus, X., Vásquez-Navarrete, J., Momboisse, F., Martinez-Quiles, N., & Cárdenas, A. M. (2017). The F-actin binding protein cortactin regulates the dynamics of the exocytotic fusion pore through its SH3 domain. *Frontiers in Cellular Neuroscience*, *11*, 130. https://doi.org/10.3389/fncel.2017.00130

Graeber, M. B., Scheithauer, B. W., & Kreutzberg, G. W. (2002). Microglia in brain tumors. *Glia*, *40*(2), 252–259. https://doi.org/10.1002/glia.10147

Gregory, J. V., Kadiyala, P., Doherty, R., Cadena, M., Habeel, S., Ruoslahti, E., Lowenstein, P. R., Castro, M. G., & Lahann, J. (2020). Systemic brain tumor delivery of synthetic protein nanoparticles for glioblastoma therapy. *Nature Communications*, *11*(1), 5687. https://doi.org/10.1038/s41467-020-19225-7

Guo, X., Pan, Y., & Gutmann, D. H. (2019). Genetic and genomic alterations differentially dictate low-grade glioma growth through cancer stem cell-specific chemokine recruitment of T cells and microglia. *Neuro-Oncology*, *21*(10), 1250–1262. https://doi.org/10.1093/neuonc/noz080

Gutmann, D. H., & Kettenmann, H. (2019). Microglia/brain macrophages as central drivers of brain tumor pathobiology. *Neuron*, *104*(3), 442–449. https://doi.org/10.1016/j.neuron.2019.08.028

Gyoneva, S., Davalos, D., Biswas, D., Swanger, S. A., Garnier-Amblard, E., Loth, F., Akassoglou, K., & Traynelis, S. F. (2014). Systemic

inflammation regulates microglial responses to tissue damage in vivo. *Glia*, *62*(8), 1345–1360. https://doi.org/10.1002/glia.22686

Hambardzumyan, D., Gutmann, D. H., & Kettenmann, H. (2015). The role of microglia and macrophages in glioma maintenance and progression. *Nature Neuroscience*, *19*(1), 20–27. https://doi.org/10.1038/nn.4185

Haynes, S. E., Hollopeter, G., Yang, G., Kurpius, D., Dailey, M. E., Gan, W.-B., & Julius, D. (2006). The P2Y12 receptor regulates microglial activation by extracellular nucleotides. *Nature Neuroscience*, *9*(12), 1512–1519. https://doi.org/10.1038/nn1805

Heo, D. K., Lim, H. M., Nam, J. H., Lee, M. G., & Kim, J. Y. (2015). Regulation of phagocytosis and cytokine secretion by store-operated calcium entry in primary isolated murine microglia. *Cellular Signalling*, *27*(1), 177–186. https://doi.org/10.1016/j.cellsig.2014.11.003

Hutter, G., Theruvath, J., Graef, C. M., Zhang, M., Schoen, M. K., Manz, E. M., Bennett, M. L., Olson, A., Azad, T. D., Sinha, R., Chan, C., Kahn, S. A., Gholamin, S., Wilson, C., Grant, G., He, J., Weissman, I. L., Mitra, S. S., & Cheshier, S. H. (2019). Microglia are effector cells of CD47-SIRPα antiphagocytic axis disruption against glioblastoma. *Proceedings of the National Academy of Sciences of the United States of America*, *116*(3), 201721434. https://doi.org/10.1073/pnas.1721434116

Hyenne, V., Ghoroghi, S., Collot, M., Bons, J., Follain, G., Harlepp, S., Mary, B., Bauer, J., Mercier, L., Busnelli, I., Lefebvre, O., Fekonja, N., Garcia-Leon, M. J., Machado, P., Delalande, F., López, A. A., Silva, S. G., Verweij, F. J., van Niel, G., & Goetz, J. G. (2019). Studying the fate of tumor extracellular vesicles at high spatiotemporal resolution using the zebrafish embryo. *Developmental Cell*, *48*(4), 554–572.e7. https://doi.org/10.1016/j.devcel.2019.01.014

Jaiswal, S., Jamieson, C. H. M., Pang, W. W., Park, C. Y., Chao, M. P., Majeti, R., Traver, D., van Rooijen, N., & Weissman, I. L. (2009). CD47 Is upregulated on circulating hematopoietic stem cells and leukemia cells to avoid phagocytosis. *Cell*, *138*(2), 271–285. https://doi.org/10.1016/j.cell.2009.05.046

Juliano, J., Gil, O., Hawkins-Daarud, A., Noticewala, S., Rockne, R. C., Gallaher, J., Massey, S. C., Sims, P. A., Anderson, A. R. A., Swanson, K. R., & Canoll, P. (2018). Comparative dynamics of microglial and glioma cell motility at the infiltrative margin of brain tumours. *Journal of The Royal Society Interface*, *15*(139), 20170582. https://doi.org/10.1098/rsif.2017.0582

Kadiyala, P., Li, D., Nuñez, F. M., Altshuler, D., Doherty, R., Kuai, R., Yu, M., Kamran, N., Edwards, M., Moon, J. J., Lowenstein, P. R., Castro, M. G., & Schwendeman, A. (2019). High-density lipoprotein-mimicking nanodiscs for chemo-immunotherapy against glioblastoma multiforme. *ACS Nano*, *2*(13), 1365–1384. https://doi.org/10.1021/acsnano.8b06842

Kanehisa, M., & Goto, S. (2000). KEGG: Kyoto Encyclopedia of genes and genomes. *Nucleic Acids Research*, *28*(1), 27–30. https://doi.org/10.1093/nar/28.1.27

Karperien, A. (2013). Quantitating the subtleties of microglial morphology with fractal analysis. *Frontiers in Cellular Neuroscience*, *3*(7), 1–18. https://doi.org/10.3389/fncel.2013.00003

Kettenmann, H., Hanisch, U.-K., Noda, M., & Verkhratsky, A. (2011). Physiology of microglia. *Physiological Reviews*, *91*(2), 461–553. https://doi.org/10.1152/physrev.00011.2010

Klemm, F., Maas, R. R., Bowman, R. L., Kornete, M., Soukup, K., Nassiri, S., Brouland, J.-P., Iacobuzio-Donahue, C. A., Brennan, C., Tabar, V., Gutin, P. H., Daniel, R. T., Hegi, M. E., & Joyce, J. A. (2020). Interrogation of the microenvironmental landscape in brain tumors reveals disease-specific alterations of immune cells. *Cell*, *181*(7), 1643–1660. https://doi.org/10.1016/j.cell.2020.05.007

Koizumi, S., Shigemoto-Mogami, Y., Nasu-Tada, K., Shinozaki, Y., Ohsawa, K., Tsuda, M., Joshi, B. V., Jacobson, K. A., Kohsaka, S., & Inoue, K. (2007). UDP acting at P2Y6 receptors is a mediator of microglial phagocytosis. *Nature*, *446*(7139), 1091–1095. https://doi.org/10.1038/nature05704

Komohara, Y., Ohnishi, K., Kuratsu, J., & Takeya, M. (2008). Possible involvement of the M2 anti-inflammatory macrophage phenotype in growth of human gliomas. *The Journal of Pathology*, *216*(1), 15–24. https://doi.org/10.1002/path.2370

Kvisten, M., Mikkelsen, V., Stensjen, A., Solheim, O., Want, J. v. d., & Torp, S. (2019). Microglia and macrophages in human glioblastomas: A morphological and immunohistochemical study. *Molecular and Clinical Oncology*, *11*(1), 31–36. https://doi.org/10.3892/mco.2019.1856

Kyrargyri, V., Madry, C., Rifat, A., Arancibia-Carcamo, I. L., Jones, S. P., Chan, V. T. T., Xu, Y., Robaye, B., & Attwell, D. (2020). P2Y13 receptors regulate microglial morphology, surveillance, and resting levels of interleukin 1β release. *Glia*, *68*(2), 328–344. https://doi.org/10.1002/glia.23719

Larson, K. C., Draper, M. P., Lipko, M., & Dabrowski, M. (2010). Gng12 is a novel negative regulator of LPS-induced inflammation in the microglial cell line BV-2. *Inflammation Research*, *59*(1), 15–22. https://doi.org/10.1007/s00011-009-0062-2

Lawson, L. J., Perry, V. H., & Gordon, S. (1992). Turnover of resident microglia in the normal adult mouse brain. *Neuroscience*, *48*(2), 405–415. https://doi.org/10.1016/0306-4522(92)90500-2

Li, F., Lv, B., Liu, Y., Hua, T., Han, J., Sun, C., Xu, L., Zhang, Z., Feng, Z., Cai, Y., Zou, Y., Ke, Y., & Jiang, X. (2017). Blocking the CD47-SIRPα axis by delivery of anti-CD47 antibody induces antitumor effects in glioma and glioma stem cells. *OncoImmunology*, *7*(2), e1391973. https://doi.org/10.1080/2162402x.2017.1391973

Li, P., Bademosi, A. T., Luo, J., & Meunier, F. A. (2018). Actin remodeling in regulated exocytosis: Toward a mesoscopic view. *Trends in Cell Biology*, *28*(9), 685–697. https://doi.org/10.1016/j.tcb.2018.04.004

Li, Q., Cheng, Z., Zhou, L., Darmanis, S., Neff, N. F., Okamoto, J., Gulati, G., Bennett, M. L., Sun, L. O., Clarke, L. E., Marschallinger, J., Yu, G., Quake, S. R., Wyss-Coray, T., & Barres, B. A. (2019). Developmental heterogeneity of microglia and brain myeloid cells revealed by deep single-cell RNA sequencing. *Neuron*, *101*(2), 207–223.e10. https://doi.org/10.1016/j.neuron.2018.12.006

Li, W., & Graeber, M. B. (2012). The molecular profile of microglia under the influence of glioma. *Neuro-Oncology*, *14*(8), 958–978. https://doi.org/10.1093/neuonc/nos116

Linder, S., Nelson, D., Weiss, M., & Aepfelbacher, M. (1999). Wiskott-Aldrich syndrome protein regulates podosomes in primary human macrophages. *Proceedings of the National Academy of Sciences of the United States of America*, *96*(17), 9648–9653. https://doi.org/10.1073/pnas.96.17.9648

Liu, Y.-J., Zhang, T., Cheng, D., Yang, J., Chen, S., Wang, X., Li, X., Duan, D., Lou, H., Zhu, L., Luo, J., Ho, M. S., Wang, X.-D., & Duan, S. (2020). Late endosomes promote microglia migration via cytosolic translocation of immature protease cathD. *Science Advances*, *6*(50), eaba5783. https://doi.org/10.1126/sciadv.aba5783

Lively, S., & Schlichter, L. C. (2013). The microglial activation state regulates migration and roles of matrix-dissolving enzymes for invasion. *Journal of Neuroinflammation*, *10*(1), 75. https://doi.org/10.1186/1742-2094-10-75

Lorenz, M., Yamaguchi, H., Wang, Y., Singer, R. H., & Condeelis, J. (2004). Imaging sites of N-WASP activity in Lamellipodia and invadopodia of carcinoma cells. *Current Biology*, *14*(8), 697–703. https://doi.org/10.1016/j.cub.2004.04.008

Love, M. I., Huber, W., & Anders, S. (2014). Moderated estimation of fold change and dispersion for RNA-seq data with DESeq2. *Genome Biology*, *15*(12), 550. https://doi.org/10.1186/s13059-014-0550-8

Lucki, N. C., Villa, G. R., Vergani, N., Bollong, M. J., Beyer, B. A., Lee, J. W., Anglin, J. L., Spangenberg, S. H., Chin, E. N., Sharma, A., Johnson, K., Sander, P. N., Gordon, P., Skirboll, S. L., Wurdak, H., Schultz, P. G., Mischel, P. S., & Lairson, L. L. (2019). A cell type-selective apoptosis-inducing small molecule for the treatment of brain cancer. *Proceedings of the National Academy of Sciences of the United States of America*, *116*(13), 201816626. https://doi.org/10.1073/pnas.1816626116

Ma, D., Liu, S., Lal, B., Wei, S., Wang, S., Zhan, D., Zhang, H., Lee, R. S., Gao, P., Lopez-Bertoni, H., Ying, M., Li, J. J., Laterra, J., Wilson, M. A., & Xia, S. (2019). Extracellular matrix protein Tenascin C increases phagocytosis mediated by CD47 loss of function in glioblastoma.

Cancer Research, *79*(10), 2697–2708. https://doi.org/10.1158/0008-5472.can-18-3125

Madry, C., Arancibia-Cárcamo, I. L., Kyrargyri, V., Chan, V. T. T., Hamilton, N. B., & Attwell, D. (2018). Effects of the ecto-ATPase apyrase on microglial ramification and surveillance reflect cell depolarization, not ATP depletion. *Proceedings of the National Academy of Sciences of the United States of America*, *115*(7), 201715354. https://doi.org/10.1073/pnas.1715354115

Madry, C., Kyrargyri, V., Arancibia-Cárcamo, I. L., Jolivet, R., Kohsaka, S., Bryan, R. M., & Attwell, D. (2018). Microglial ramification, surveillance, and Interleukin-1β release are regulated by the two-pore Domain K+ Channel THIK-1. *Neuron*, *97*(2), 299–312.e6. https://doi.org/10.1016/j.neuron.2017.12.002

Marion, S., Mazzolini, J., Herit, F., Bourdoncle, P., Kambou-Pene, N., Hailfinger, S., Sachse, M., Ruland, J., Benmerah, A., Echard, A., Thome, M., & Niedergang, F. (2012). The NF-κB signaling protein Bcl10 regulates actin dynamics by controlling AP1 and OCRL-bearing vesicles. *Developmental Cell*, *23*(5), 954–967. https://doi.org/10.1016/j.devcel.2012.09.021

Markovic, D. S., Glass, R., Synowitz, M., van Rooijen, N., & Kettenmann, H. (2005). Microglia stimulate the invasiveness of glioma cells by increasing the activity of metalloprotease-2. *Journal of Neuropathology & Experimental Neurology*, *64*(9), 754–762. https://doi.org/10.1097/01.jnen.0000178445.33972.a9

May, R. C., Caron, E., Hall, A., & Machesky, L. M. (2000). Involvement of the Arp2/3 complex in phagocytosis mediated by FcγR or CR3. *Nature Cell Biology*, *2*(4), 246–248. https://doi.org/10.1038/35008673

Mayrhofer, M., Gourain, V., Reischl, M., Affaticati, P., Jenett, A., Joly, J.-S., Benelli, M., Demichelis, F., Poliani, P. L., Sieger, D., & Mione, M. (2017). A novel brain tumour model in zebrafish reveals the role of YAP activation in MAPK- and PI3K-induced malignant growth. *Disease Models & Mechanisms*, *10*(1), 15–28. https://doi.org/10.1242/dmm.026500

Mazzolini, J., Chia, K., & Sieger, D. (2018). Isolation and RNA extraction of neurons macrophages and microglia from larval zebrafish. *Brains*, *134*, e57431. https://doi.org/10.3791/57431

Mazzolini, J., Clerc, S. L., Morisse, G., Coulonges, C., Kuil, L. E., Ham, T. J., Zagury, J. F., & Sieger, D. (2019). Gene expression profiling reveals a conserved microglia signature in larval zebrafish. *Glia*, *68*(2), 298–315. https://doi.org/10.1002/glia.23717

Mazzolini, J., Herit, F., Bouchet, J., Benmerah, A., Benichou, S., & Niedergang, F. (2010). Inhibition of phagocytosis in HIV-1-infected macrophages relies on Nef-dependent alteration of focal delivery of recycling compartments. *Blood*, *115*(21), 4226–4236. https://doi.org/10.1182/blood-2009-12-259473

Murray, R. Z., Kay, J. G., Sangermani, D. G., & Stow, J. L. (2005). A role for the phagosome in cytokine secretion. *Science*, *310*(5753), 1492–1495. https://doi.org/10.1126/science.1120225

Neumann, H., Kotter, M. R., & Franklin, R. J. M. (2008). Debris clearance by microglia: An essential link between degeneration and regeneration. *Brain: A Journal of Neurology*, *132*(Pt 2), 288–295. https://doi.org/10.1093/brain/awn109

Niedergang, F., & Grinstein, S. (2018). How to build a phagosome: new concepts for an old process. *Current Opinion in Cell Biology*, *50*, 57–63. https://doi.org/10.1016/j.ceb.2018.01.009

Nimmerjahn, A., Kirchhoff, F., & Helmchen, F. (2005). Resting microglial cells are highly dynamic surveillants of brain parenchyma in vivo. *Science*, *308*(5726), 1314–1318. https://doi.org/10.1126/science.1110647

Noda, M., Takii, K., Parajuli, B., Kawanokuchi, J., Sonobe, Y., Takeuchi, H., Mizuno, T., & Suzumura, A. (2014). FGF-2 released from degenerating neurons exerts microglial-induced neuroprotection via FGFR3-ERK signaling pathway. *Journal of Neuroinflammation*, *11*(1), 76. https://doi.org/10.1186/1742-2094-11-76

Norris, G. T., Smirnov, I., Filiano, A. J., Shadowen, H. M., Cody, K. R., Thompson, J. A., Harris, T. H., Gaultier, A., Overall, C. C., & Kipnis, J. (2018). Neuronal integrity and complement control synaptic material clearance by microglia after CNS injury. *Journal of Experimental Medicine*, *215*(7), 1789–1801. https://doi.org/10.1084/jem.20172244

Okazaki, T., Saito, D., Inden, M., Kawaguchi, K., Wakimoto, S., Nakahari, T., & Asano, S. (2020). Moesin is involved in microglial activation accompanying morphological changes and reorganization of the actin cytoskeleton. *The Journal of Physiological Sciences*, *70*(1), 52. https://doi.org/10.1186/s12576-020-00779-6

Olivares, M. J., González-Jamett, A. M., Guerra, M. J., Baez-Matus, X., Haro-Acuña, V., Martínez-Quiles, N., & Cárdenas, A. M. (2014). Src kinases regulate de novo actin polymerization during exocytosis in neuroendocrine chromaffin cells. *PLoS ONE*, *9*(6), e99001. https://doi.org/10.1371/journal.pone.0099001

Ory, S., & Gasman, S. (2011). Rho GTPases and exocytosis: What are the molecular links? *Seminars in Cell & Developmental Biology*, *22*(1), 27–32. https://doi.org/10.1016/j.semcdb.2010.12.002

Park, H., & Cox, D. (2009). Cdc42 regulates Fcγ receptor-mediated phagocytosis through the activation and phosphorylation of Wiskott-Aldrich syndrome protein (WASP) and neural-WASP. *Molecular Biology of the Cell*, *20*(21), 4500–4508. https://doi.org/10.1091/mbc.e09-03-0230

Peri, F., & Nüsslein-Volhard, C. (2008). Live imaging of neuronal degradation by microglia reveals a role for v0-ATPase a1 in phagosomal fusion in vivo. *Cell*, *133*(5), 916–927. https://doi.org/10.1016/j.cell.2008.04.037

Pollard, T. D., & Cooper, J. A. (2009). Actin, a central player in cell shape and movement. *Science (New York, N.Y.)*, *326*(5957), 1208–1212. https://doi.org/10.1126/science.1175862

Pyonteck, S. M., Akkari, L., Schuhmacher, A. J., Bowman, R. L., Sevenich, L., Quail, D. F., Olson, O. C., Quick, M. L., Huse, J. T., Teijeiro, V., Setty, M., Leslie, C. S., Oei, Y., Pedraza, A., Zhang, J., Brennan, C. W., Sutton, J. C., Holland, E. C., Daniel, D., & Joyce, J. A. (2013). CSF-1R inhibition alters macrophage polarization and blocks glioma progression. *Nature Medicine*, *19*(10), 1264–1272. https://doi.org/10.1038/nm.3337

Quail, D. F., & Joyce, J. A. (2017). The microenvironmental landscape of brain tumors. *Cancer Cell*, *31*(3), 326–341. https://doi.org/10.1016/j.ccell.2017.02.009

Resende, F. F. B., Bai, X., Bel, E. A. D., Kirchhoff, F., Scheller, A., & Titze-de-Almeida, R. (2016). Evaluation of TgH(CX3CR1-EGFP) mice implanted with mCherry-GL261 cells as an in vivo model for morphometrical analysis of glioma-microglia interaction. *BMC Cancer*, *16*(72), 1–13. https://doi.org/10.1186/s12885-016-2118-3

Ricard, C., Tchoghandjian, A., Luche, H., Grenot, P., Figarella-Branger, D., Rougon, G., Malissen, M., & Debarbieux, F. (2016). Phenotypic dynamics of microglial and monocyte-derived cells in glioblastoma-bearing mice. *Scientific Reports*, *6*(1), 26381. https://doi.org/10.1038/srep26381

Santoriello, C., Gennaro, E., Anelli, V., Distel, M., Kelly, A., Köster, R. W., Hurlstone, A., & Mione, M. (2010). Kita driven expression of oncogenic HRAS leads to early onset and highly penetrant melanoma in zebrafish. *PLoS ONE*, *5*(12), e15170. https://doi.org/10.1371/journal.pone.0015170

Sassa, T., Aizawa, H., & Okamoto, H. (2007). Visualization of two distinct classes of neurons by gad2 and zic1 promoter/enhancer elements in the dorsal hindbrain of developing zebrafish reveals neuronal connectivity related to the auditory and lateral line systems. *Developmental Dynamics*, *236*(3), 706–718. https://doi.org/10.1002/dvdy.21084

Schwayer, C., Sikora, M., Slováková, J., Kardos, R., & Heisenberg, C.-P. (2016). Actin rings of power. *Developmental Cell*, *37*(6), 493–506. https://doi.org/10.1016/j.devcel.2016.05.024

Schwickert, A., Weghake, E., Brüggemann, K., Engbers, A., Brinkmann, B. F., Kemper, B., Seggewiß, J., Stock, C., Ebnet, K., Kiesel, L., Riethmüller, C., & Götte, M. (2015). microRNA miR-142-3p inhibits breast cancer cell invasiveness by synchronous targeting of WASL, integrin Alpha V, and additional cytoskeletal elements. *PLOS ONE*, *10*(12), e0143993. https://doi.org/10.1371/journal.pone.0143993

Sieger, D., Moritz, C., Ziegenhals, T., Prykhozhij, S., & Peri, F. (2012). Long-range Ca2+ waves transmit brain-damage signals to microglia. *Developmental Cell*, *22*(6), 1138–1148. https://doi.org/10.1016/j.devcel.2012.04.012

Simmons, G. W., Pong, W. W., Emnett, R. J., White, C. R., Gianino, S. M., Rodriguez, F. J., & Gutmann, D. H. (2011). Neurofibromatosis-1 heterozygosity increases microglia in a spatially and temporally restricted pattern relevant to mouse optic glioma formation and growth. *Journal of Neuropathology and Experimental Neurology*, *70*(1), 51–62. https://doi.org/10.1097/nen.0b013e3182032d37

Svahn, A. J., Graeber, M. B., Ellett, F., Lieschke, G. J., Rinkwitz, S., Bennett, M. R., & Becker, T. S. (2013). Development of ramified microglia from early macrophages in the zebrafish optic tectum. *Developmental Neurobiology*, *73*(1), 60–71. https://doi.org/10.1002/dneu.22039

Svitkina, T. (2018). The actin cytoskeleton and actin-based motility. *Cold Spring Harbor Perspectives in Biology*, *10*(1), a018267. https://doi.org/10.1101/cshperspect.a018267

Tkach, M., & Théry, C. (2016). Communication by extracellular vesicles: Where we are and where we need to go. *Cell*, *164*(6), 1226–1232. https://doi.org/10.1016/j.cell.2016.01.043

Tsarouchas, T. M., Wehner, D., Cavone, L., Munir, T., Keatinge, M., Lambertus, M., Underhill, A., Barrett, T., Kassapis, E., Ogryzko, N., Feng, Y., van Ham, T. J., Becker, T., & Becker, C. G. (2018). Dynamic control of proinflammatory cytokines Il-1β and Tnf-α by macrophages in zebrafish spinal cord regeneration. *Nature Communications*, *9*(1), 4670. https://doi.org/10.1038/s41467-018-07036-w

Uhlemann, R., Gertz, K., Boehmerle, W., Schwarz, T., Nolte, C., Freyer, D., Kettenmann, H., Endres, M., & Kronenberg, G. (2015). Actin dynamics shape microglia effector functions. *Brain Structure and Function*, *221*(5), 2717–2734. https://doi.org/10.1007/s00429-015-1067-y

Underhill, D. M., & Ozinsky, A. (2002). Phagocytosis of microbes: Complexity in action. *Annual Review of Immunology*, *20*(1), 825–852. https://doi.org/10.1146/annurev.immunol.20.103001.114744

Verweij, F. J., Revenu, C., Arras, G., Dingli, F., Loew, D., Pegtel, D. M., Follain, G., Allio, G., Goetz, J. G., Zimmermann, P., Herbomel, P., Bene, F. D., Raposo, G., & van Niel, G. (2019). Live tracking of inter-organ communication by endogenous exosomes in vivo. *Developmental Cell*, *48*(4), 573–589.e4. https://doi.org/10.1016/j.devcel.2019.01.004

Voisin, P., Bouchaud, V., Merle, M., Diolez, P., Duffy, L., Flint, K., Franconi, J.-M., & Bouzier-Sore, A.-K. (2010). Microglia in close vicinity of glioma cells: Correlation between phenotype and metabolic alterations. *Frontiers in Neuroenergetics*, *2*, 131. https://doi.org/10.3389/fnene.2010.00131

van der Vos, K. E., Abels, E. R., Zhang, X., Lai, C., Carrizosa, E., Oakley, D., Prabhakar, S., Mardini, O., Crommentuijn, M. H. W., Skog, J., Krichevsky, A. M., Stemmer-Rachamimov, A., Mempel, T. R., Khoury, J. E., Hickman, S. E., & Breakefield, X. O. (2015). Directly visualized glioblastoma-derived extracellular vesicles transfer RNA to microglia/macrophages in the brain. *Neuro-Oncology*, *18*(1), 58–69. https://doi.org/10.1093/neuonc/nov244

Wang, H., Zhang, L., Zhang, I. Y., Chen, X., Fonseca, A. D., Wu, S., Ren, H., Badie, S., Sadeghi, S., Ouyang, M., Warden, C. D., & Badie, B. (2013). S100B promotes glioma growth through chemoattraction of myeloid-derived macrophages. *Clinical Cancer Research*, *19*(14), 3764–3775. https://doi.org/10.1158/1078-0432.ccr-12-3725

Wang, Q., Hu, B., Hu, X., Kim, H., Squatrito, M., Scarpace, L., de Carvalho, A. C., Lyu, S., Li, P., Li, Y., Barthel, F., Cho, H. J., Lin, Y.-H., Satani, N., Martinez-Ledesma, E., Zheng, S., Chang, E., Sauvé, C.-E. G., Olar, A., … Verhaak, R. G. W. (2017). Tumor evolution of glioma-intrinsic gene expression subtypes associates with immunological changes in the microenvironment. *Cancer Cell*, *32*(1), 42–56.e6. https://doi.org/10.1016/j.ccell.2017.06.003

Wang, Q.-C., Wan, X., Jia, R.-X., Xu, Y., Liu, X., Zhang, Y., & Sun, S.-C. (2020). Inhibition of N-WASP affects actin-mediated cytokinesis during porcine oocyte maturation. *Theriogenology*, *144*, 132–138. https://doi.org/10.1016/j.theriogenology.2020.01.005

Wen, P. Y., & Kesari, S. (2008). Malignant gliomas in adults. *The New England Journal of Medicine*, *359*(5), 492–507. https://doi.org/10.1056/nejmra0708126

Wu, A., Wei, J., Kong, L. Y., Wang, Y., Priebe, W., Qiao, W., Sawaya, R., & Heimberger, A. B. (2010). Glioma cancer stem cells induce immunosuppressive macrophages/microglia. *Neuro-Oncology*, *12*(11), 1113–1125. https://doi.org/10.1093/neuonc/noq082

Xiang, Z., Lv, Q., Chen, X., Zhu, X., Liu, S., Li, D., & Peng, X. (2020). Lnc GNG12-AS1 knockdown suppresses glioma progression through the AKT/GSK-3β/β-catenin pathway. *Bioscience Reports*, *40*(8), BSR20201578. https://doi.org/10.1042/bsr20201578

Yamaguchi, H., Lorenz, M., Kempiak, S., Sarmiento, C., Coniglio, S., Symons, M., Segall, J., Eddy, R., Miki, H., Takenawa, T., & Condeelis, J. (2005). Molecular mechanisms of invadopodium formation. *The Journal of Cell Biology*, *168*(3), 441–452. https://doi.org/10.1083/jcb.200407076

Yu, X., Zech, T., McDonald, L., Gonzalez, E. G., Li, A., Macpherson, I., Schwarz, J. P., Spence, H., Futó, K., Timpson, P., Nixon, C., Ma, Y., Anton, I. M., Visegrády, B., Insall, R. H., Oien, K., Blyth, K., Norman, J. C., & Machesky, L. M. (2012). N-WASP coordinates the delivery and F-actin–mediated capture of MT1-MMP at invasive pseudopodsN-WASP in 3D cancer cell invasion. *The Journal of Cell Biology*, *199*(3), 527–544. https://doi.org/10.1083/jcb.201203025

Zhai, H., Heppner, F. L., & Tsirka, S. E. (2011). Microglia/macrophages promote glioma progression. *Glia*, *59*(3), 472–485. https://doi.org/10.1002/glia.21117

Zhang, J., Sarkar, S., Cua, R., Zhou, Y., Hader, W., & Yong, V. W. (2012). A dialog between glioma and microglia that promotes tumor invasiveness through the CCL2/CCR2/interleukin-6 axis. *Carcinogenesis*, *33*(2), 312–319. https://doi.org/10.1093/carcin/bgr289

Zhang, Y., Chen, K., Sloan, S. A., Bennett, M. L., Scholze, A. R., O'Keeffe, S., Phatnani, H. P., Guarnieri, P., Caneda, C., Ruderisch, N., Deng, S., Liddelow, S. A., Zhang, C., Daneman, R., Maniatis, T., Barres, B. A., & Wu, J. Q. (2014). An RNA-sequencing transcriptome and splicing database of glia, neurons, and vascular cells of the cerebral cortex. *The Journal of Neuroscience*, *34*(36), 11929–11947. https://doi.org/10.1523/jneurosci.1860-14.2014

Zhang, Y., Sloan, S. A., Clarke, L. E., Caneda, C., Plaza, C. A., Blumenthal, P. D., Vogel, H., Steinberg, G. K., Edwards, M. S. B., Li, G., Duncan, J. A., Cheshier, S. H., Shuer, L. M., Chang, E. F., Grant, G. A., Gephart, M. G. H., & Barres, B. A. (2016). Purification and characterization of progenitor and mature human astrocytes reveals transcriptional and functional differences with mouse. *Neuron*, *89*(1), 37–53. https://doi.org/10.1016/j.neuron.2015.11.013

SUPPORTING INFORMATION

Additional supporting information may be found in the online version of the article at the publisher's website.

How to cite this article: Mazzolini, J., Le Clerc, S., Morisse, G., Coulonges, C., Zagury, J.-F., & Sieger, D. (2022). Wasl is crucial to maintain microglial core activities during glioblastoma initiation stages. *Glia*, *70*(6), 1027–1051. https://doi.org/10.1002/glia.24154